Journal of Materiomics 5 (2019) 15–33

Contents lists available at ScienceDirect

Journal of Materiomics

journal homepage: www.journals.elsevier.com/journal-of-materiomics/

Thermoelectric properties of silicon and recycled silicon sawing waste

Ran He [a, *], Wieland Heyn [a, b], Felix Thiel [a], Nicolás Pérez [a], Christine Damm [a], Darius Pohl [a, c], Bernd Rellinghaus [a, c], Christian Reimann [d], Maximilian Beier [d], Jochen Friedrich [d], Hangtian Zhu [e], Zhifeng Ren [e], Kornelius Nielsch [a, b], Gabi Schierning [a, **]

[a] Leibniz-Institut für Festkörper- und Werkstoffforschung Dresden, 01069, Dresden, Germany
[b] Institute of Materials Science, Technische Universität Dresden, 01069, Dresden, Germany
[c] Dresden Center for Nanoanalysis, Technische Universität Dresden, 01062, Dresden, Germany
[d] Fraunhofer Institut für Integrierte Systeme und Bauelementetechnologie, 91058, Erlangen, Germany
[e] Department of Physics and TcSUH, University of Houston, Houston, TX, 77204, USA

ARTICLE INFO

Article history:
Received 22 August 2018
Received in revised form
30 October 2018
Accepted 5 November 2018
Available online 14 November 2018

Keywords:
Silicon
Thermoelectric
Nanostructure
Power factor
Sawing waste

ABSTRACT

Large-scale-applicable thermoelectric materials should be both self-sustaining, in order to survive long-term duty cycles, and nonpolluting. Among all classes of known thermoelectric materials, these criteria reduce the available candidate pool, leaving silicon as one of the remaining options. Here we first review the thermoelectric properties of various silicon-related materials with respect to their morphologies and microstructures. We then report the thermoelectric properties of silicon sawing wastes recycled from silicon wafer manufacturing. We obtain a high power factor of ~32 $\mu W\,cm^{-1}\,K^{-2}$ at 1273 K with 6% phosphorus substitution in the Si crystal, a value comparable to that of phosphorus-doped silicon-germanium alloys. Our work suggests the large-scale thermoelectric applicability of recycled silicon that would otherwise contribute to the millions of tons of industrial waste produced by the semiconductor industry.

Contents

* Corresponding author.
** Corresponding author.
E-mail addresses: r.he@ifw-dresden.de (R. He), g.schierning@ifw-dresden.de (G. Schierning).

Peer review under responsibility of The Chinese Ceramic Society.

https://doi.org/10.1016/j.jmat.2018.11.004

1. Introduction: thermoelectric, *zT*, and power factor

The concepts of the *smart electric grid* and *distributed energy resources* require supplying power to customers in a clean, efficient, and tailored fashion, along with partial replacement of the centralized grid. Great challenges must be overcome to realize such innovations. For example, the availability of clean energy from multiple sources such as solar, wind, geothermal, *etc.* is restricted by natural conditions such as nighttime, wind inconsistency, and reservoir depletion. Although assisting technologies such as supercapacitors, phase change materials, and advanced batteries can be installed to mitigate the instability of the power supply, these clean energy technologies still cannot compete with the central grid in terms of reliability and stability. Additionally, in remote areas such as the polar regions, deserts, isolated islands, and tropical rainforests that the central power grid cannot reach and where infrastructure construction is difficult, long-term reliable and maintenance-free power generation is highly desired.

Thermoelectric (TE) generators (TEGs) have proven their reliability in generating power. When used in conjunction with an operating device, they can convert some of its wasted heat into electricity, thereby improving its efficiency, and reducing its fuel consumption. In comparison to other candidate techniques for waste-heat recovery, such as organic Rankine cycles [1,2] or thermogalvanics [3,4], TE devices are unique due to their solid-state nature. They are reliable, noiseless, scalable, and maintenance-free. As a practical application, radioisotope thermoelectric generators (RTGs) have powered space missions for decades without a single failure, which demonstrates the extraordinary reliability of TEGs in power generation. The drawback of the TEG is its relatively low efficiency due to the limited performance of TE materials and high material costs. Therefore, it is crucial to boost the performance of TE materials or to significantly reduce their costs.

For an ideal TE device in which the heat can be supplied and removed effectively and with negligible contact losses, the heat-to-power conversion efficiency (η) can be expressed as

$$\eta = \frac{T_H - T_C}{T_H} \cdot \frac{\sqrt{1+\overline{zT}} - 1}{\sqrt{1+\overline{zT}} + \frac{T_C}{T_H}} \tag{1}$$

where $\overline{zT}$ is the average TE figure of merit (zT) between the hot-side temperature (T_H) and the cold-side temperature (T_C) of a TE material, and is defined as

$$zT = \frac{PF}{\kappa}T \tag{2}$$

$$PF = S^2 \Big/ \rho \tag{3}$$

$$\kappa = \kappa_L + \kappa_e + \kappa_{bip} \tag{4}$$

where *PF*, *T*, κ, *S*, ρ, κ_L, κ_e, and κ_{bip} are the power factor, absolute temperature, total thermal conductivity, Seebeck coefficient, electrical resistivity, lattice thermal conductivity, electronic thermal conductivity, and bipolar thermal conductivity, respectively. Consequently, a higher *zT* corresponds to higher conversion efficiency.

Despite the recent developments in TE materials research, however, commercially available TE devices are still based on a limited material set, mostly the Bi_2Te_3 compounds [5]. Therefore, TE applications are currently restricted to niche markets where the need for reliability outweighs the need for conversion efficiency. To realize further *zT* improvement, approaches are necessary to suppress the thermal conductivity (κ), especially the lattice thermal conductivity (κ_L), or to boost the power factor (*PF*). In the past decade, *zT* enhancement has been mainly achieved by suppressing the κ_L using methods such as point defect scattering, nanostructuring, and lattice anharmonicity [6–10]. However, the low κ often originates as the result of weak chemical bonding, and therefore the mechanical strength of many TE materials is an inherent aspect to be considered. Moreover, the thermal conductivity of many TE materials is already approaching the amorphous limits, so its further suppression seems unrealistic.

In comparison to the reduction of phonon thermal conductivity, improving *zT* by boosting the *PF* has not been widely studied [11–15]. Unlike the approach of lowering thermal conductivity, increasing *PF* yields no adverse effects. The output power density ω, which is as important as *zT*, is determined by the average *PF* as

$$\omega = \frac{(T_H - T_C)^2}{4l}\overline{PF} \tag{5}$$

where *l* is the leg length. The importance of high *PF* was recently experimentally confirmed in half-Heusler compounds, where output power density of ~22 W cm^{-2} has been realized [14,16].

In recent years, there have been reports of significant improvements in the *zT* values of a variety of TE materials such as Bi_2Te_3 [8,17–22], Skutterudites [23–28], IV-VI compounds [29–40], half-Heuslers [41–51], Mg_2(Si,Ge,Sn) [13,52–55], Zintl phases [15,56–65], MgAgSb [66–72], $AgSbTe_2$ [9,73,74], Liquid-like materials [75–78], *etc.*, as summarized in Fig. 1a and b. Peak *zT* exceeding 2 and average *zT* exceeding 1 have been frequently reported. On the other hand, the applicability of many TE materials, such as SnSe, is limited due to the low *PF* values, as shown in Fig. 1c and d. The successful combination of both high *PF* and high *zT* has been realized in only a limited number of material systems, such as half-Heuslers, SiGe alloys, Skutterudites, Bi_2Te_3, and GeTe compounds. However, the applicability of these materials is further restricted by factors such as the chemical stability of the compounds, as well as the scarcity of the related elements (Hf, Bi, Te). Based on these considerations, the half-Heusler and SiGe alloys would be the first-choice candidates for possible power generation applications at mid-to-high temperatures.

Meanwhile silicon (Si), the second-most abundant element in the earth's crust, shows impressive potential for being an applicable TE material because of its low price, excellent chemical and mechanical stability, non-toxicity, and high industrial compatibility. As a widely studied semiconductor, both n- and p-type properties have been realized in Si, which greatly facilitates the

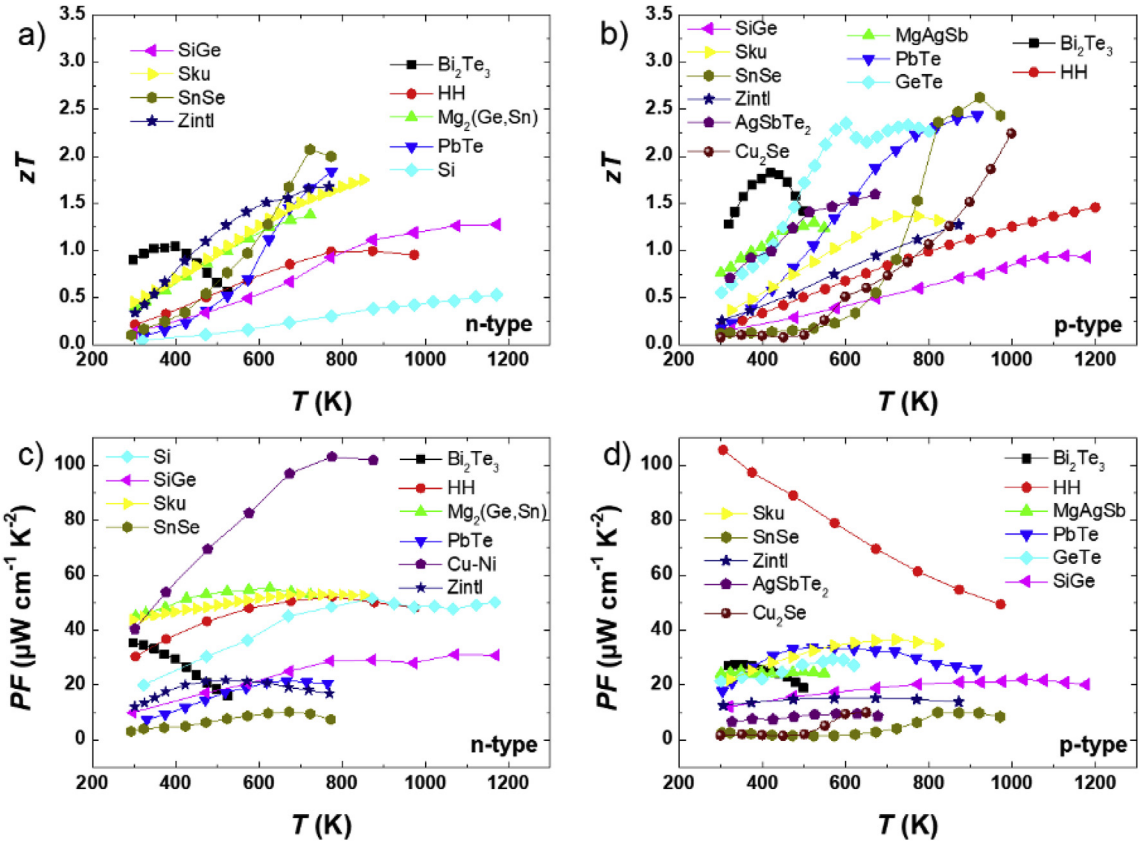

Fig. 1. Comparisons of a-b) *zT* and c-d) power factors of selected a,c) n-type and b,d) p-type TE materials above room temperature. N-type: repressed $Bi_2Te_{2.7}Se_{0.3}$ [20], $Cu_{56}Ni_{42}Mn_2$ [81], $Mg_2Sn_{0.75}Ge_{0.25}$ [53], Si [79], 0.2%Co/$Ba_{0.3}In_{0.3}Co_4Sb_{12}$ [Skutterudite (Sku)] [27], $Mg_{3.1}Co_{0.1}Sb_{1.5}Bi_{0.49}Te_{0.01}$ (Zintl) [58], $Hf_{0.5}Zr_{0.5}NiSn_{0.99}Sb_{0.01}$ [half-Heusler (HH)] [82], PbTe-4% InSb [83], SnSe-Bi [84], and $Si_{80}Ge_{20}P_2$ [85]. P-type: $AgSbTe_2$ [74], liquid-phase-sintered $Bi_{0.5}Sb_{1.5}Te_3$ [19], $Cu_{1.94}Se_{0.5}S_{0.5}$ [75], $Ge_{0.86}Pb_{0.1}Bi_{0.04}Te$ [33], Nb_{1-x} (Hf,Ti)$_x$FeSb (HH) [14,48], SnSe [35], $Mg_{0.99}Li_{0.01}Ag_{0.97}Sb_{0.99}$ [69], PbTe-SrTe [86], $La_{0.8}Ti_{0.1}Ga_{0.1}Fe_{3.3}Co_{0.7}Sb_{12}$ [25], $Eu_{0.2}Yb_{0.2}Ca_{0.6}Mg_2Bi_2$ (Zintl) [56], and $Si_{80}Ge_{20}B_5$ [87].

engineering process in building TE devices. In terms of TE properties, excellent *PF*s of ~50 μW cm^{-1} K^{-2} were realized with phosphorus (P)-doping in a wide temperature range from 500 to 900 °C [79], as shown in Fig. 1c. Such *PF* is much higher than that of many other good TE materials. However, single-crystalline Si is barely considered as a promising TE material due to its high thermal conductivity (κ) of ~150 W m^{-1} K^{-1} at 300 K [80]. Suppressing the thermal conductivity of Si is of utmost importance to enhance its TE performance, and, as will be discussed below, this has been realized through approaches such as Ge-substitution, nano-bulk structuring, low dimensionality, *etc*.

In the 1990s, the concept of nanostructuring was proposed by Dresselhaus and Hicks [88,89], and has subsequently achieved continued great success in the TE field up until now. The nanostructuring concept has mainly two branches. The first is utilizing the quantum confinement effect, where the electronic density of states can be adjusted to enhance *PF* [90]. The confined interfaces present individual scattering behavior to electrons and phonons, thus allowing at least partial decoupling of the transport of both. The second is constructing nano-bulk structures so that the bulk material contains nano-sized structures that can impede phonon transport [79,91]. By applying the first approach, Si nanowires showed ultrahigh *zT* values of ~1 at a relatively low temperature of ~200 K–300 K [92,93]. Such high values of *zT* were mainly achieved through a substantial suppression of κ by two orders of magnitude with intensified phonon scattering from the nanowire boundaries. On the other hand, nano-bulk structures also showed the potential to intensify the phonon scattering, with an improved *zT* value of ~0.7 reported in nano-bulk-structured n-type Si at ~1200 K [94]. These studies not only demonstrate the effectiveness of phonon scattering, but have also greatly encouraged the TE community to apply the nanostructure concepts to further enhance the performance of TE materials.

In this article, we dedicate section 2 to summarizing the TE performance of Si-related materials. Approaches such as Ge alloying, nano-bulk structuring, modulation doping, and dimension manipulation, as well as the corresponding effects, especially those for phonon impeding, will be discussed in detail. This review will mainly focus on the experimental results, and theoretical discussion will be introduced only when necessary. In section 3, we discuss the TE performance of recycled Si obtained from the wire sawing waste from the production of single-crystalline silicon wafers. A high PF of ~32 μW cm^{-1} K^{-2} is realized through heavy P–doping, and a peak *zT* value of ~0.33 is obtained at 1273 K. We highlight the promising potential of recycled Si for TE applications at high temperatures considering the thermal stability, high abundance, and very low cost of the source material.

2. TE properties of Si-related materials

2.1. Alloying with Ge

Although the pure elemental Si and Ge single crystals possess high thermal conductivity, as shown in Fig. 2a, SiGe alloys show strong effects in impeding phonon transport. Typically, these alloys were prepared by zone leveling in the 1960s [95–97], and have been prepared by hot pressing (HP) beginning in the 1970s due to the simplicity and time effectiveness of the method [98–103]. The

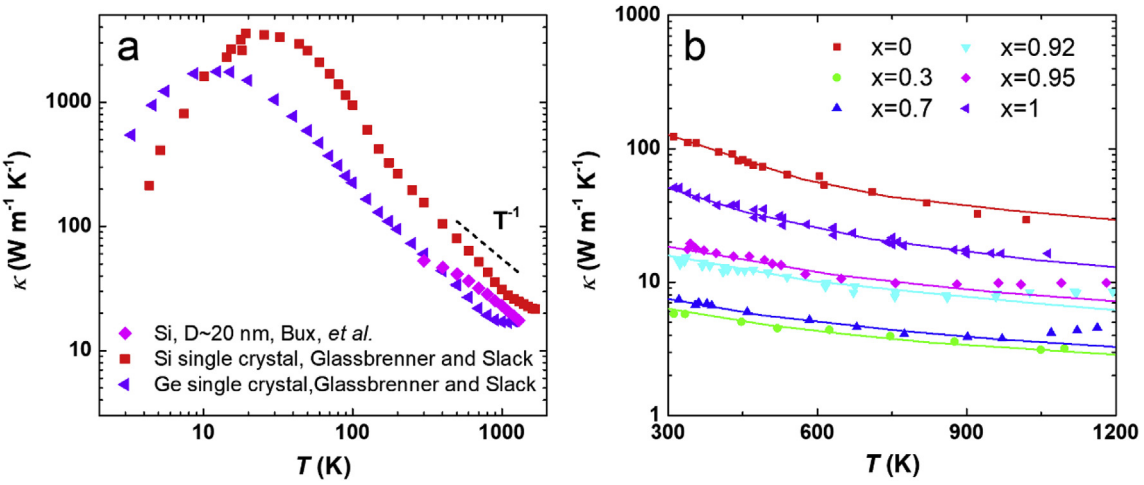

Fig. 2. a) Thermal conductivity of Si and Ge [80,94]. b) Thermal conductivity of undoped polycrystalline $Si_{1-x}Ge_x$ alloys [96]. The dashed line in a) shows the T^{-1} relation of thermal conductivity to absolute temperature.

prepared samples are polycrystalline with grain size on the order of millimeters to centimeters. Fig. 2b shows the thermal conductivity of $Si_{1-x}Ge_x$ alloys prepared by such an approach. A huge suppression of thermal conductivity was obtained with a Ge concentration up to 30%. Further substitution of Ge does not yield a significant change in thermal conductivity until x>70%, when the thermal conductivity increases again. Klemens [104] and Abeles [105] concluded that the dramatic decrease of the lattice thermal conductivity originates from the mass fluctuation between Si and Ge, as well as from an increased anharmonicity of phonon-phonon interaction due to the alloying effect.

The suppressed thermal conductivity in SiGe alloys suggests great beneficial effects in boosting the TE performance. N– and p-type properties of SiGe alloys could be realized by doping with elements such as phosphorus (P) and boron (B), respectively. The typical TE properties for both types of $Si_{80}Ge_{20}$ alloys are shown in Fig. 3 [103]. As shown by Dismukes et al., doping not only increases the number of carriers, but also intensifies phonon scattering through electron-phonon interaction [95]. Such an effect was also calculated from first-principles in Si by Liao et al. [106]. Peak *zT* values reaching ~0.65 and ~1 in p- and n-type $Si_{80}Ge_{20}$, respectively, were repeatedly realized at 900 °C–950 °C in different studies [95,102,103,105,107–110]. Additionally, in another composition, $Si_{85}Ge_{15}$, with less Ge content, peak *zT* values of ~0.74 and ~1 were realized in p- and n-type alloys at ~1200 K [95,111,112].

2.2. Nano-bulk structure

2.2.1. Nano-bulk structure in SiGe alloys

We previously mentioned three mechanisms for blocking phonon transport: anharmonic phonon-phonon scattering, point-defect scattering, and electron-phonon interaction. However, the thermal conductivity values of SiGe alloys (~4 $W m^{-1} K^{-1}$) remain much higher than the amorphous limit of ~1 $W m^{-1} K^{-1}$ reported by Cahill and Pohl [113]. Further thermal conductivity suppression requires additional scattering centers, such as grain boundaries. In fact, the strategy of boundary scattering to impede phonon transport trace back to Goldsmid and Penn [114], and the first experimental evidence was provided by Rowe et al. who sintered n-type $Si_{63.5}Ge_{36.5}$ with a similar carrier concentration (1×10^{20} cm^{-3}) and high density above 98%, but with different grain sizes varying from less than 5 μm–25 μm [102]. The sintered alloys with grain sizes of less than 5 μm possess decreased lattice thermal conductivity of 28% at 300 K compared to the zone-leveled materials. An exhaustive study was subsequently performed by Vining et al., in which 28 $Si_{80}Ge_{20}$ samples that were heavily doped with either P or B were synthesized with grain sizes varying between 1 μm and 100 μm [103]. The phonon thermal conductivity showed a drop as large as ~37% in the sample with the smallest grains in comparison with the zone-leveled sample. However, the *zT* did not increase accordingly due to the simultaneously enhanced scattering of charge carriers.

Thus it seemed that grain-size reduction is not beneficial to the TE performance of SiGe alloys. However, in 2008, Wang et al. and Joshi et al. reported substantial improvement in TE performance of the n- and p-type $Si_{80}Ge_{20}$ alloys, respectively, by constructing nanocrystalline-structured bulk (nano-bulk structure) materials in which the grain sizes were decreased down to the sub-micron level [85,87]. In a typical experiment, the elemental Si, Ge, and dopant (B or P) were weighed according to stoichiometry, and then a high-energy ball milling process was applied to the elements to synthesize the alloy powders as well as to decrease the grain size. As shown in Fig. 4, the synthesized powders are single-phase with typical grain sizes of less than 20 nm [87]. Subsequently, the ball-milled powder was sintered in a quick hot-press process, usually at 950–1200 °C and under 60–80 MPa for 2–5 min. The sintered composites have a grain size of ~20 nm, as shown in Fig. 5a and b. Moreover, the nanograins of the sintered samples are highly crystalline, randomly oriented, and closely packed, and have very clean boundaries (Fig. 5c and d).

Fig. 3 shows the TE properties of both types of nano-bulk $Si_{80}Ge_{20}$ alloys. The nano-bulk structure only slightly affects the resistivity (Fig. 3a) and the Seebeck coefficient (Fig. 3b), while it greatly suppresses the thermal conductivity (Fig. 3c). Thus the *zT* values of these alloys are significantly improved, with peak values reaching 1.3 and 1.0 for n-type and p-type materials, respectively (Fig. 3d). In comparison to the bulk $Si_{80}Ge_{20}$ alloy, the relative enhancement reaches 30% and 70% for n- and p-type materials, respectively.

It was proposed that the suppressed thermal conductivity in nano-bulk structured SiGe alloys emerges from the difference in the mean-free path between electrons (~1–10 nm) and phonons (~1–10 μm) [108]. Therefore, the grain boundaries are expected to strongly scatter the phonon transport while only slightly impeding the electron transport. This explanation sounds plausible, but it does not match the results obtained by Vining et al., who found that the grain boundary scatters electrons to the same extent that it

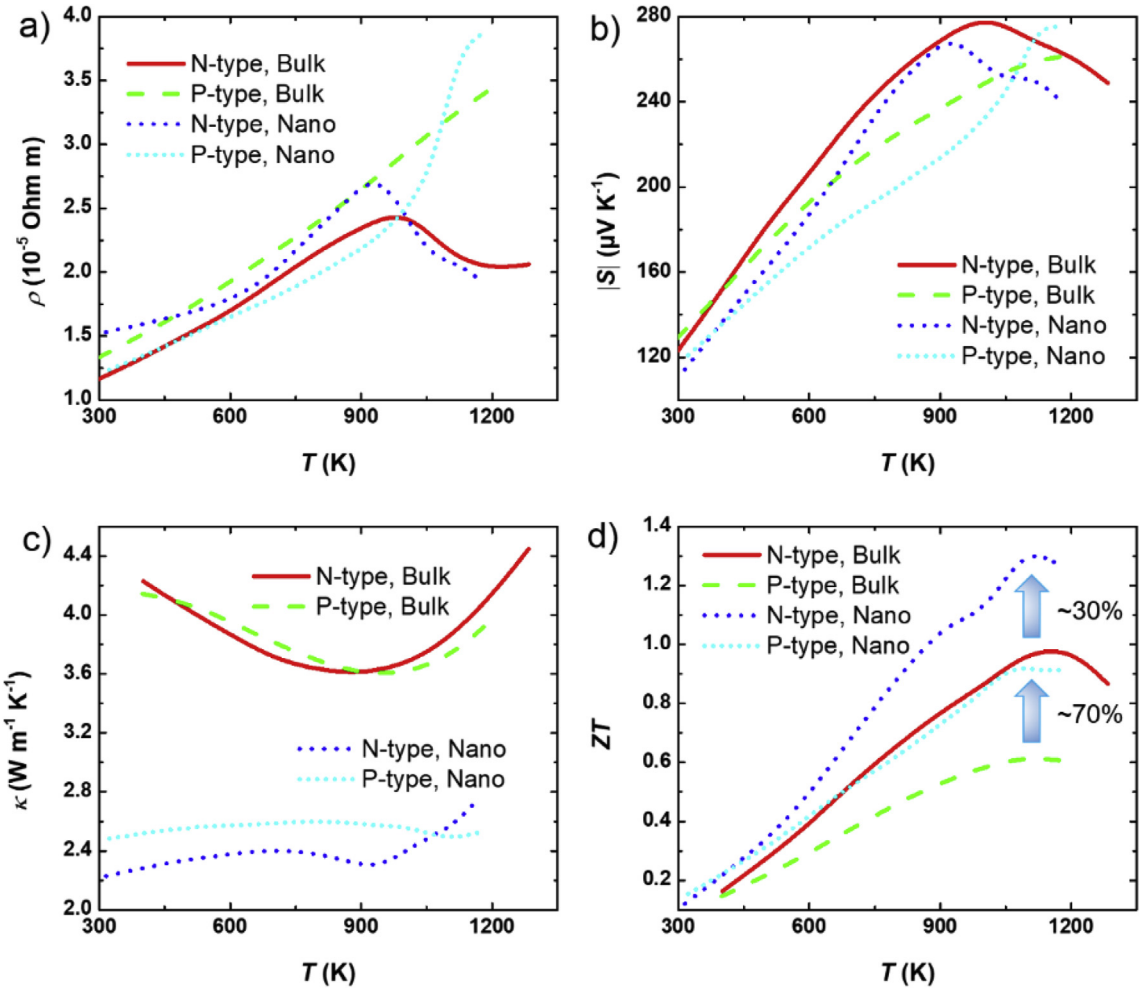

Fig. 3. Typical thermoelectric properties, a) resistivity, b) Seebeck coefficient, c) thermal conductivity, and d) *zT*, of typical n- and p-type bulk and nano-bulk $Si_{80}Ge_{20}$ [85,87,103].

scatters phonons, even though the grain sizes are much larger (5 μm and above) than the electron mean-free path [103]. Instead of treating the boundary region as inertial to electron transport, we suggest that it is more reasonable to consider the boundaries as transport channels for charge carriers. Therefore, the increased number of transport channels for the charge carriers may compensate for the stronger boundary scattering when grain sizes are small enough, *i.e.* the surface-to-volume ratio is larger. Indeed, boundary charge transport is widely known in Si [115]. However, further investigation is required to experimentally analyze such trade-offs.

2.2.2. Nano-bulk structure in Si

Even without alloying Si with Ge, the nano-bulk concept alone boosts the TE performance of elemental Si. Bux et al. experimentally synthesized Si with phosphorus (P) doping through high energy ball milling and sintering [94]. Powders with grain size of ~20 nm were obtained. The subsequent sintering increased the grain size to ~50–100 nm, while nanocrystalline domains of 10–20 nm were still present. As a result, the lattice thermal conductivity was significantly suppressed to 6.2 $W m^{-1} K^{-1}$ at room temperature, and to 3 $W m^{-1} K^{-1}$ at 1200 K. The suppression of lattice thermal conductivity is remarkable in comparison to the Si single crystal (150 $W m^{-1} K^{-1}$ at room temperature). As shown in Fig. 6, the low lattice thermal conductivity leads to a high *zT* value of 0.7 at 1200 K. A similar high *zT* of 0.6 was obtained at 1125 K with 6% P substitution in Si by Zhu et al. [116]. It should be noted that it was predicted that maximum *zT* values of nearly 1.0 could be achieved if the grain size could be further reduced to 10 nm [117]. Considering the high price of Ge, further reducing the grain size of nanocrystalline Si to enhance its TE performance deserves investigation.

Although milled Si material exhibits good TE performance, the milling process route has some drawbacks such as the potential risk for unwanted incorporation of impurities and a limit due to the lowest achievable particle size. As an alternative method, Schierning et al. used the gas-phase process to obtain nano-sized Si powders [120–122]. The schematics of the gas-phase synthesis are shown in Fig. 7. This bottom-up technique is an economical way to manufacture nanocrystalline powders without the intermediate steps of milling a bulk material. Most importantly, gas-phase synthesis has the advantages of controllable particle sizes from a few nm up to the μm size, as well as homogeneous doping within a very broad range during the synthesis. It thus opens the way for direct synthesis of materials with an optimized composition and size with respect to their TE properties. An upscaling of the applied gas phase synthesis for industrial processes has already been demonstrated, with nanopowder output on the order of kgs per day [123].

The as-prepared Si nanopowders were further processed by using a spark plasma sintering (SPS) machine. A peak *zT* of 0.5 was obtained at 950 °C for a sample sintered at 1060 °C with a mean crystalline size of 46 nm [120]. Similar results were reported by

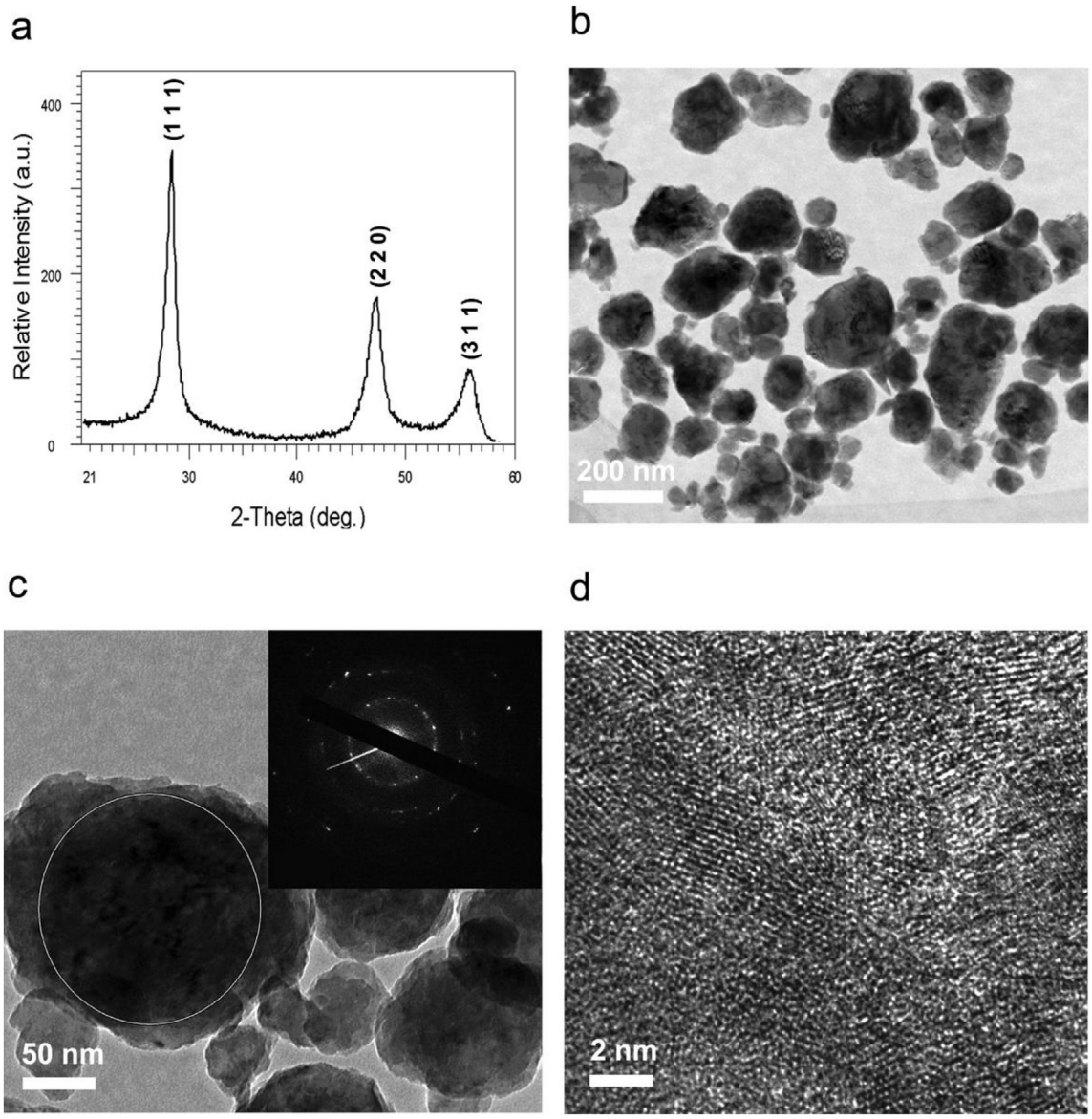

Fig. 4. (a) XRD pattern and TEM images with (b) low, (c) medium, and (d) high magnifications of the ball-milled $Si_{80}Ge_{20}$ nanopowders. The inset in panel (c) is the selected area electron diffraction rings to show the multicrystalline nature of an individual particle [87]. Reprinted with permission from Giri Joshi et al., Nano Lett., Vol. 8, No. 12, 2008. Copyright 2008 American Chemical Society.

Claudio et al., who found that the sintered sample preserved the nanocrystalline character with grain size varying between 48 and 264 nm from TEM observation [118]. The samples present a significantly decreased lattice thermal conductivity to 25 $W m^{-1} K^{-1}$, which, in combination with a very high carrier mobility, resulted in a *zT* with a competitive value that peaks at *zT* ~0.57 at 973 °C.

For the p-type counterpart, Kessler et al. produced boron-doped silicon nanoparticles by a continuous gas-phase process and compacted the nanoparticles into nanocomposites by SPS sintering. The maximum *zT* value of the p-type Si nanocomposites is ~0.3 at 700 °C with an average crystalline size between 40 and 80 nm [119]. The *zT*s of nano-bulk Si from several studies are summarized in Fig. 6.

2.3. Modulation doping

High-performance thermoelectric materials, including SiGe alloys, are usually heavily doped semiconductors in which guest atoms replace the atoms of the base compound, change the carrier concentration, and therefore tune the TE performance. However, the ionization of dopant atoms yields the ionized centers, which inevitably scatter electrons so that the carrier mobility is suppressed. This disadvantage can be overcome by the concept of modulation doping. Modulation doping has been widely used in thin-film semiconductors that separate the charge carriers from the ionized dopants to reduce the charge scattering and to increase the carrier mobility. This ultimately leads to an increased electrical conductivity [124]. Zebarjadi et al. and Yu et al. introduced the concept to three-dimensional bulk SiGe alloys and improved their power factor as well as their figure of merit [125,126]. As schematically shown in Fig. 8, modulation-doped samples are made from two types of nanograins (a two-phase composite), where dopants are incorporated into only one type. Band engineering allows charge carriers to be separated from their parent grains and moved into the undoped grains, which results in enhanced mobility

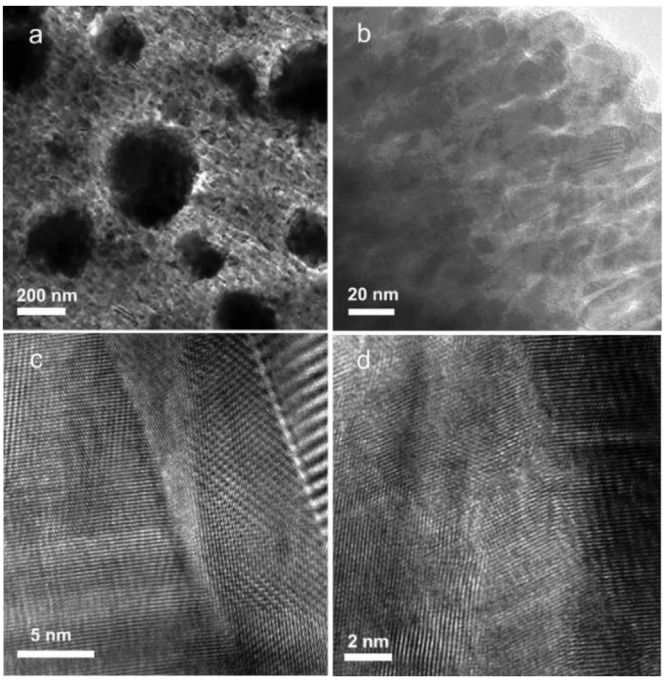

Fig. 5. Transmission electron microscopy (TEM) images of the typical dc hot-pressed nanostructured dense bulk samples at (a) low, (b) medium, and (c,d) high magnifications [87]. Reprinted with permission from Giri Joshi et al., Nano Lett., Vol. 8, No. 12, 2008. Copyright 2008 American Chemical Society.

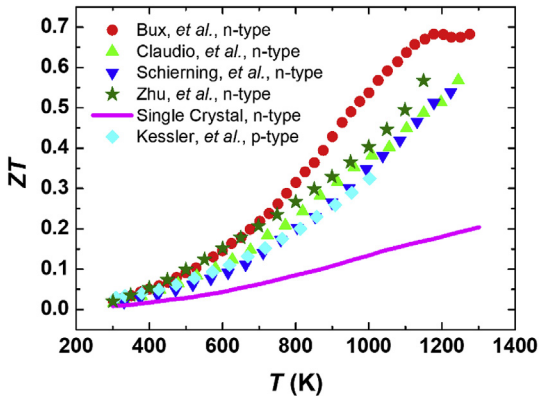

Fig. 6. Comparison of zT as a function of temperature for different Si materials. The zT of single-crystalline n-type Si is also plotted for comparison [94,116,118–120].

of the carriers in comparison to uniform doping due to a reduction of ionized impurity scattering.

Comparisons of the electrical conductivity, the Seebeck coefficient, and the power factor of the modulation-doped and the equivalent uniformly doped SiGe alloys are shown in Fig. 9 for both n-type (a, b, and c) and p-type (d, e, and f) compounds [125]. The corresponding compositions are $(Si_{80}Ge_{20})_{80}(Si_{100}P_3)_{20}$, $Si_{84}Ge_{16}P_{0.6}$, $(Si_{80}Ge_{20})_{70}(Si_{100}B_5)_{30}$, and $Si_{86}Ge_{14}B_{1.5}$ for n-type modulation doping, n-type uniform doping, p-type modulation doping, and p-type uniform doping, respectively. Clearly, the electrical conductivity of modulation-doped compounds is significantly higher than that of the uniformly doped ones (Fig. 9a and d). As reported by Zebarjadi et al., the increase in electrical conductivity originates from an enhanced carrier mobility [125]. Although the Seebeck coefficient drops slightly with modulation doping (Fig. 9b and e), the power factor still increases, which is clearly due to the overcompensation from the increased electrical conductivity (Fig. 9c and f). However, in the study by Zebarjadi et al., modulation-doped compounds also possess higher thermal conductivity with pure Si being employed as the matrix [125]. Therefore, the overall zT did not enhance significantly [125]. In another study by Yu et al., the alloy $Si_{70}Ge_{30}$, rather than Si, was employed as the doped compound and $Si_{95}Ge_5$ as the matrix [126]. This combination is effective in both improving the power factor as well as suppressing the thermal conductivity. The zT is thus enhanced from 1.0 to 1.3 at 900 °C in comparison to the uniformly doped $Si_{86.25}Ge_{13.75}P_{1.05}$ and modulation-doped $(Si_{95}Ge_5)_{0.65}(Si_{70}Ge_{30}P_3)_{0.35}$ that have identical elemental constitution.

2.4. Low-dimensional Si

The strategy of using low dimensionality to enhance the TE performance was theoretically initiated by Hicks and Dresselhaus [88,89]. Soon afterward, concepts such as carrier pocket engineering [127,128], energy filtering [129], and the semimetal-semiconductor transition [130] were realized in material systems such as SiGe, PbTe, and Bi, and the beneficial effects were experimentally observed. These reports stimulated great interest in the study of TE performance of low-dimensional materials. Various nano structures of silicon have been realized and their TE properties have been studied, including nanowires, nanolayers, phononic structures, *etc*.

2.4.1. Si nanowire

In 2008, Hochbaum et al. and Boukai et al. reported high zT values of ~0.6 and ~1 at 300 K and 200 K, respectively, in silicon nanowires [92,93]. These enhanced zT values mainly originate from a huge suppression of κ by ~2 orders of magnitude with a low value reaching ~1 W m^{-1} K^{-1} at 200–250 K, which is even lower than the amorphous limit of Si [131]. The mechanisms for such reductions in κ were not fully understood, but possible reasons were proposed, including 1) increased boundary scattering, 2) an altered phonon dispersion relation, and 3) quantization of phonon transport due to the decreased characteristic sizes [132]. It should be noted that these exceptionally low thermal conductivity values were also the subject of a critical discussion in the TE community [133]. To understand the underlying mechanisms, Li et al. measured the thermal conductivity of Si nanowires with diameters from 22 to 115 nm. They found that between 20 and 60 K, the exponent of the temperature dependence in κ changed from ~T^3 for thick nanowires to ~T^1 for thin nanowires [132]. The κ~T^3 relation in thick nanowires suggests a dominant role for boundary scattering in phonon transport, such that the thermal conductivity follows the temperature dependence of the specific heat. However, the observed κ~T^1 relation in nanowires as thin as 22 nm suggests that other scattering mechanisms dominate. The κ~T^1 relation was theoretically reproduced by Chen et al. by incorporating the frequency-dependent phonon-boundary scattering that originates from the surface roughness [134]. In addition, a variety of models and simulations were subsequently built to rationalize the experimental data, yielding a general consensus that surface roughness influences the conduction of phonons [135–143].

While these theoretical investigations shed light on the roughness-dependent κ of Si nanowires, the final experimental evidence was provided by Lim et al., who quantified the effects of surface roughness on phonon transport using TEM observations [144]. Lim et al. drew the following conclusions: 1) the root-mean-square of surface roughness exhibits a more pronounced impact on the thermal conductivity than the diameter, and 2) the thermal conductivity clearly shows a variation trend with a parameter α_q, which is obtained from a power law behavior of the roughness

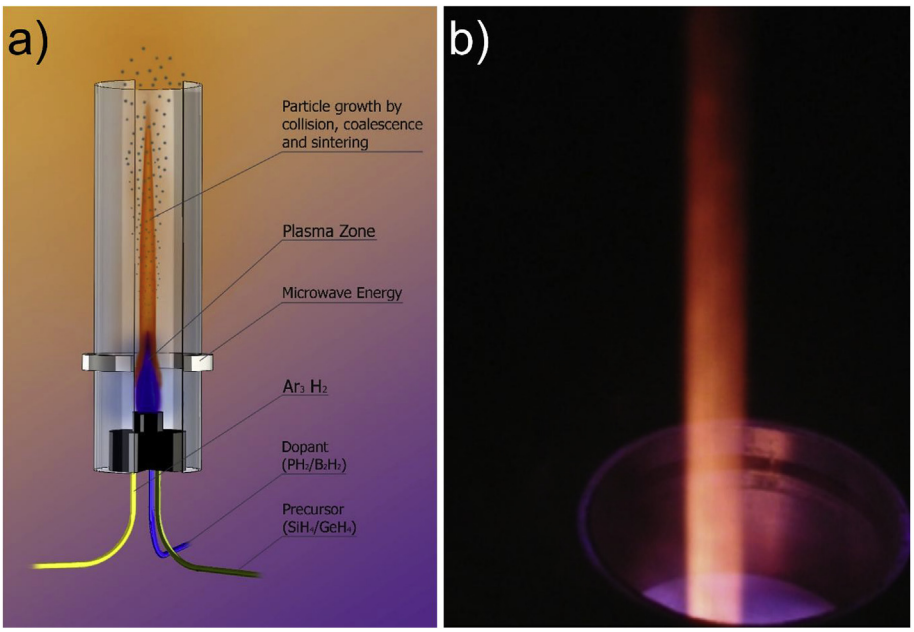

Fig. 7. a) Sketch of the gas-phase synthesis for doped silicon nanoparticles. The precursors silane (SiH_4) and phosphine (PH_3) decompose within a microwave-induced Ar/H_2 plasma. The shape of the nanoparticles can be tailored by parameters such as gas pressure, flow rates, microwave energy, and chemical composition of the gas mixture [120]. b) Photograph of the reactor in operation. It should be noted that the plasma itself can hardly be seen (purple luminescence at the bottom), and that the bright glow originates from the hot nanoparticles leaving the plasma zone and cooling down rapidly [122]. Reprinted from Nils Petermann et al., J. Phys. D: Appl. Phys. 44 (2011) 174034, with the permission of IOP Publishing Ltd.

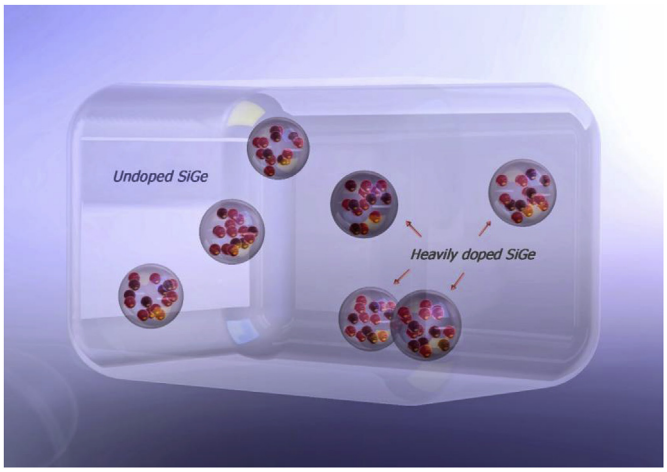

Fig. 8. Schematics of modulation doping [112].

power spectrum by Fourier transformation of the spatial correlation function [144].

Despite the feasibility of suppressing the thermal conductivity, it is challenging to translate the Si nanowires into applicable TE devices without the growth of large-area Si nanowire arrays. In recent years Si nanowire arrays (SNA) were successfully synthesized and the TE performance was studied [145–150]. Zhang et al. synthesized boron-doped Si nanowire arrays with an area of $30 \times 30\ mm^2$ using a simple metal-assisted chemical etching method with controllable morphologies such as lengths, porosities, and heterogeneous diameters [151]. The TE properties of the SNA-Si-SNA sandwich-structured composites were measured at room temperature and zT values for the corresponding porous Si nanowire arrays were obtained. The results suggested beneficial effects from the increased nanowire porosity such as enhancing the Seebeck coefficient and reducing the thermal conductivity to $1.68\ W\ m^{-1}\ K^{-1}$. As a result, a high zT of ~0.5 at 300 K was obtained [151], which is a promising result with regard to the applicability of Si nanowire arrays.

2.4.2. Si nanolayer

In comparison to the measurement of thermal conductivity of Si nanowires that can be realized through suspending the wires with micro-fabricated microstructures [93,132], measurements of thermal conductivity of Si nanolayers require different techniques such as Raman spectroscopy [152,153], time-domain thermoreflectance (TDTR) [154], frequency-domain thermoreflectance (FDTR) [155], and thermal transient grating (TTG) [156]. Similar to the results in Si nanowire, the thermal conductivity of Si nanolayer/film/membrane follows a general trend: the thinner the layer, the lower the thermal conductivity and the higher the zT [157–160]. Single-crystalline Si shows room-temperature thermal conductivities of $75\ W\ m^{-1}\ K^{-1}$, $22\ W\ m^{-1}\ K^{-1}$, and $9\ W\ m^{-1}\ K^{-1}$ at layer thickness of 74 nm, 20 nm, and 9 nm, respectively [161–163]. In polycrystalline Si nanolayers, the suppression of thermal conductivity was also observed. Zhou et al. showed a suppressed thermal conductivity of $12\ W\ m^{-1}\ K^{-1}$ in a poly-Si nanolayer with 52 nm thickness [157], and zT values of 0.067 and 0.024 were obtained at room temperature with n- and p-type doping, respectively. In comparison, the poly-Si layers with a thickness of 0.5 μm and above possess a zT of ~0.02 and ~0.01 in n- and p-type compounds, respectively [157,164,165].

Bennett and co-authors proposed another strategy to enhance the thermoelectric performance of Si nanolayers [166]. In their work, dislocation loops and extended crystallographic defects were introduced in p-type Si nanolayers through ion-implantation. These defects yield reductions in electrical conductivity, carrier concentration, and carrier mobility. However, the Seebeck coefficient increases dramatically, possibly due to the energy filtering effect caused by the defects. As a result, an improved power factor of ~66 $\mu W\ cm^{-1}\ K^{-2}$ was obtained at 300 K, which is 70% higher

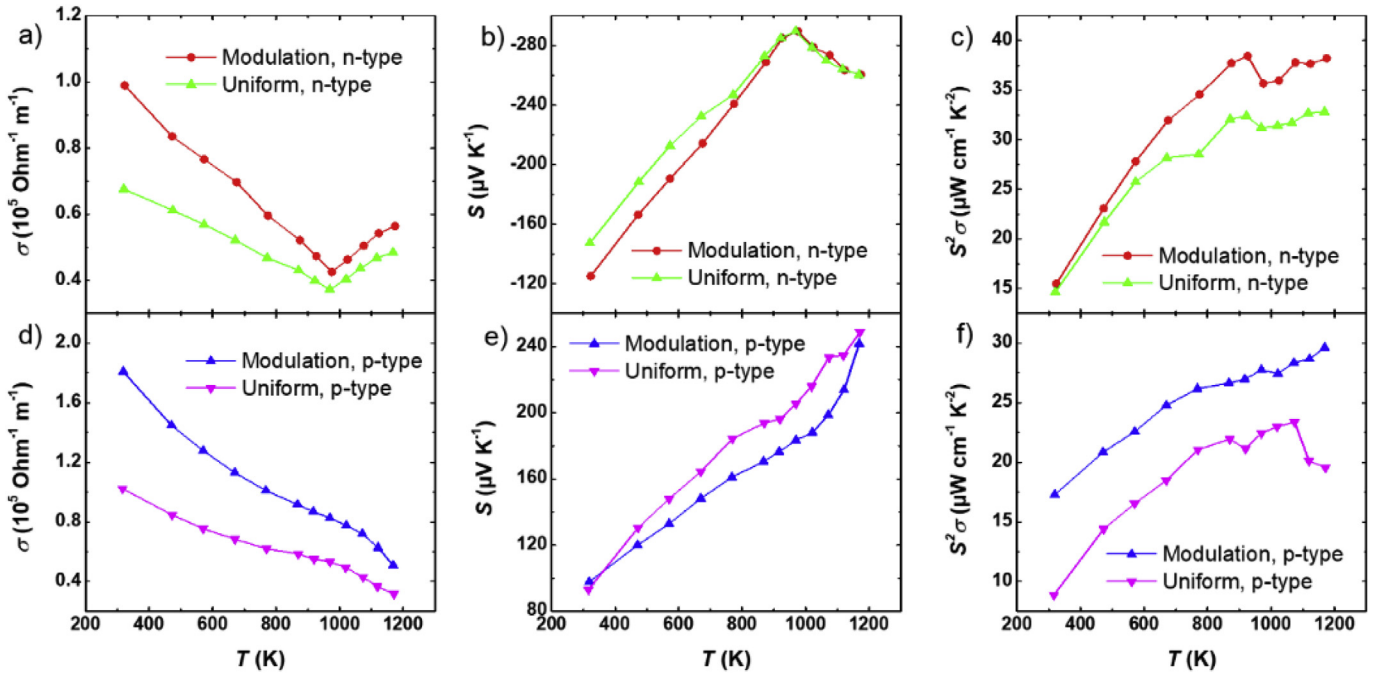

Fig. 9. Temperature dependence of thermoelectric properties of n-type (a, b, and c) and p-type (d, e, and f) modulation-doped and uniformly doped SiGe alloys. a) and d), electrical conductivity; b) and e), Seebeck coefficient; and c) and f), power factor. The corresponding compositions for n-type modulation doping, n-type uniform doping, p-type modulation doping, and p-type uniform doping are $(Si_{80}Ge_{20})_{80}(Si_{100}P_3)_{20}$, $Si_{84}Ge_{16}P_{0.6}$, $(Si_{80}Ge_{20})_{70}(Si_{100}B_5)_{30}$, and $Si_{86}Ge_{14}B_{1.5}$, respectively.

than that of bulk silicon [166]. Notably, this strategy of power-factor enhancement has the potential to be employed for bulk Si materials if the high-density dislocations can be introduced.

2.4.3. Phononic structure

Along with nanowires and nanolayers, the phononic structure of Si also shows non-trivial TE performance. A few research groups have studied the thermal conductivity of Si with phononic nanomesh structures, which can essentially be considered as acoustic metamaterials [167–171]. In general, materials with phononic structures show lower thermal conductivities, as one would expect from Boltzmann transport equations, including solely the boundary scattering. For example, Tang et al. synthesized holey Si from Si membranes by either nanosphere or block-copolymer lithography with different pitches of hexagonal holey patterns down to 55 nm [171]. They demonstrated a phonon-glass behavior with great suppression of the thermal conductivity to as low as 1.14 $W m^{-1} K^{-1}$ in 55 nm pitch holey Si at room temperature and, as a result, zT of ~0.4 was realized at room temperature. According to Dechaumphai and Chen, the unusual reduction of thermal conductivity can be understood by treating phonons with a mean-free path smaller than the characteristic size of phononic crystals as particles, whereas phonons with a mean-free path larger that the characteristic size of phononic crystals are treated as waves [172]. Subsequently, phonons with short wavelengths were analyzed by using the Boltzmann transport equation incorporating the boundary scattering, while long wavelength phonons are affected by the zone-folding effects. This model successfully reproduced the experimental results and thus highlighted the importance of the zone-folding effect on thermal transport in phononic crystals, which is essentially related to the periodicity of the micro patterning.

Instead of nanomesh structures that periodically remove a part of the Si membrane, effects of additive patterning were also studied on the phonon transport. For example, Davis and Hussein calculated the phonon dispersion relation and thermal conductivity of Si thin films with and without periodic pillar extrusions [173]. Although the number of phonon modes increases with the added pillars, the final thermal conductivity is suppressed by ~50%. Recently, Maire et al. reported the reduction of thermal conductivity in fishbone-structured Si by 20%, with the possible reason being the trapping of phonon vibration in the wings [174].

2.4.4. Other structures

The reduction of thermal conductivity was also realized in Si/Ge superlattices that consist of periodically alternating layers of Si and Ge. In general, the thermal conductivity of superlattices is comparable to that of the homogeneous alloy with an equivalent composition in the in-plane direction [175], and significant reduction of thermal conductivity in superlattices is usually realized in the cross-plane direction [176–178]. Yang et al. observed the thermal conductivity ratio of ~5 between the in-plane and cross-plane directions at 480 K [179]. The cross-plane thermal conductivity of Si/Ge superlattices was suppressed to 1–2 $W m^{-1} K^{-2}$ from 80 to 400 K [176]. Despite the reduction in thermal conductivity, there are no conclusive results on zT because of difficulties in measuring the electronic transport properties of very thin films.

Meanwhile the in-plane thermal conductivity can be further decreased by applying the rolling-up techniques [180,181]. Li et al. reported the in-plane thermal conductivity of the Si/SiO_x hybrid nanomembrane superlattices[167]. Fig. 10a shows the schematic procedures of synthesizing such rolled-up structures. The Ge sacrificial layer was pre-deposited on the substrates, and the Si/SiO_x superlattices were deposited subsequently. The interface between Ge and the Si/SiO_x are strained due to the mismatch of lattice parameter. Upon removing the Ge sacrificial layer, the rolled-up structure forms through releasing the strain. Specifically, the rolled-up superlattices with 5 windings were mechanically compressed into a planar structure, as also shown in Fig. 10a. Fig. 10b shows the morphologies of the structures through SEM observations. Fig. 10c shows the micro-device for thermal transport measurement. As shown in Fig. 10d, The in-plane thermal conductivity

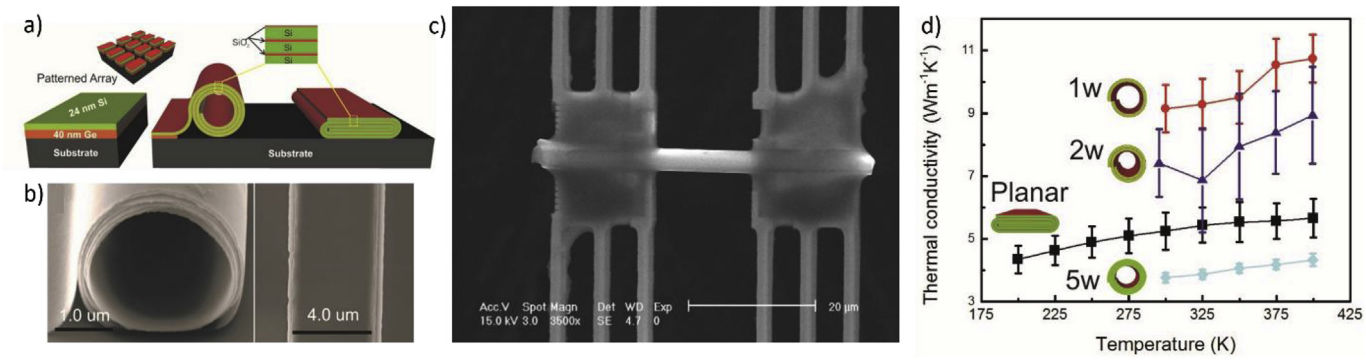

Fig. 10. a) Schematics of the synthesis procedure and structures of rolled-up and planar Si/SiO_x hybrid nanomembrane superlattices. b) SEM image of rolled-up (left) and planar (right) Si/SiO_x superlattices. c) SEM image of a representative device for thermal conductivity measurement. d) Temperature-dependent thermal conductivities of rolled-up Si/SiO_x superlattices with 1, 2, and 5 windings, and planar superlattices with 5 windings [167]. Reprinted with permission from Guodong Li et al., ACS Nano 2017, 11, 8215–8222. Copyright 2017 American Chemical Society.

was reduced from 7.64 $W\,m^{-1}\,K^{-1}$ to 3.28 $W\,m^{-1}\,K^{-1}$ at 300 K by increasing the winding number from 1 to 5 [167]. The planar structure has slightly higher thermal conductivity. This can be understood by the fact that the thermal adhesion among different windings becomes better after mechanically compressing the tubes into the planar structures. Tight adhesion among different layers improves the phonon transport processes at the interfaces and hence the corresponding in-plane thermal conductivities increase. It should be noted that the reported in-plane thermal conductivity is the lowest among the silicon-based superlattices. Moreover, unlike the situation of the cross-plane direction, measurement of electrical conductivity and Seebeck coefficient is feasible for the rolled-up superlattices, and thus their thermoelectric properties deserve further investigation.

3. Turning waste into profit: TE properties of recycled Si

3.1. Introduction

The global photovoltaic module production capacity was over 100 GW in 2017, and the Si-wafer-based photovoltaic technology accounted for more than 90% of the total production of all absorber materials [182]. Due to the escalating market requirements, the production of Si wafers has been increasing by 25–50% each year since 2000 [183]. On the other hand, in 2017, about 31% of the total cost for a photovoltaic module originated from the manufacturing and material costs of the Si wafers [182,184]. Meanwhile, cutting silicon wafers from the single-crystalline or multi-crystalline ingots relies on either a loose abrasive cutting technology in which silicon carbide (SiC)-based sawing slurries are used together with a moving steel wire or a fixed abrasive cutting technique in which resin-bonded or -plated diamonds are fixed directly on the moving steel wire [185]. The schematic of silicon wafer manufacturing is shown in Fig. 11. During wafering, a so-called Si kerf is produced, yielding a loss of about 40% of the Si feedstock [186,187]. Depending on the wafering approach employed, different kinds of used Si slurries are obtained. The obtained Si slurries contain impurities such as SiC or diamond particles from the abrasives, metals from the steel wire, and, in most cases, oxidized silicon. In total, more than 100,000 tons of this Si kerf is generated worldwide annually [188]. Taking into account an initial price of about 15–20 US$ per kg for the original high-quality Si feedstock used for crystal growth, it could be stated that Si material of around 2 billion US$ per year is ground down to small Si particles in form of the Si kerf. Therefore, the cost of Si

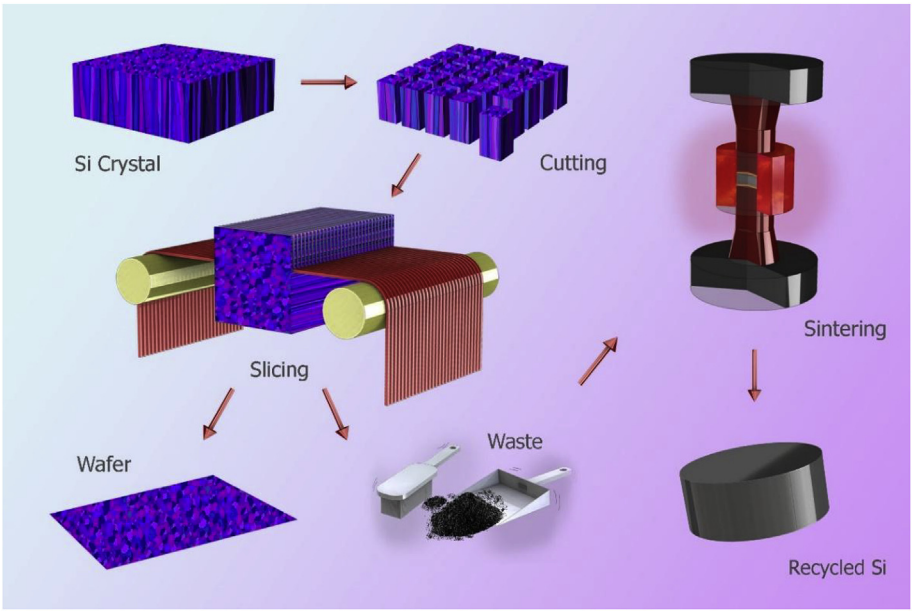

Fig. 11. Wafer manufacturing steps and waste silicon recycling.

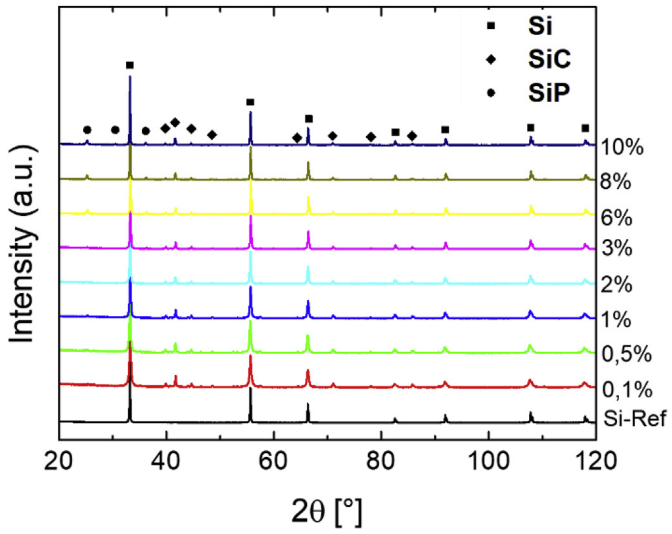

Fig. 12. XRD measurements of silicon slurry with different amounts of P content.

wafer production could be partly recovered upon turning these wastes into profits. Currently, the research direction regarding recycling these sawing wastes is mainly focused on the recovery of the used coolant (water or polyethylene glycol) as well as the used SiC particles. In recent years, some attention has also been paid to the recycling of the Si particles [188].

The use of recycled Si in thermoelectric applications has also been proposed as another potential strategy to reduce the cost of silicon wafer manufacturing. The high cost of TE-generated power might be mitigated by using low (close to zero)-cost feedstocks for the TEGs, stimulating interest in recycled Si as a material for TE applications. For example, Akasaka et al. and Honda et al. investigated the TE properties of Mg_2Si synthesized using Si obtained from recycled sawing waste and peak zT values of 0.5–0.6 were obtained at 800–860 K [189,190]. Recently, Isoda et al. [191] and Mesaritis et al. [192] synthesized $Mg_2(Si,Ge,Sn)$ compounds using purified Si kerf as the starting material. They obtained similar TE performance in comparison to that of compounds synthesized from commercial-grade high-purity silicon. These reports demonstrated the great potential of using Si kerf for thermoelectric applications. Here we report the direct translation of recycled Si into TE materials using techniques that are industrially mature, such as mechanical alloying and SPS. As a result, a high PF of ~32 μW cm^{-1} K^{-2} is obtained at 1273 K with 6% P substitution of Si. The obtained PF is comparable to that of the $Si_{80}Ge_{20}$ alloys that are widely synthesized for building TEGs. Additionally, the obtained peak zT reaches ~0.33, suggesting the potential of recycled Si kerf for TE power generation applications at high temperatures considering the abundance and low cost of the source material.

3.2. Results and discussion

The Si obtained from recycling of the sawing waste was originally produced by a European wafer manufacturer that used the loose abrasive technique based on SiC particles and the coolant polyethylene glycol. The as-obtained Si batches after recycling are mixtures of several elements/compounds. Depending on the detailed recycling process technology, the mixtures typically contain Si (70–85 wt%), SiC (15–30 wt%), metals (up to 5 wt%), and oxidized silicon or metal phases. In this study, the Si recycling batch consists of 78 wt% Si and 22 wt% SiC, which converts to the mole ratio of 71.66% Si to 28.34% SiC, and to the volumetric ratio of 83% Si to 17% SiC (for details of the batch composition comparison, see Table S1 in the supplementary information). Phosphorus (P) was chosen as the dopant to tune the carrier concentration. It should be noted that the solubility of P in SiC is negligible in comparison to

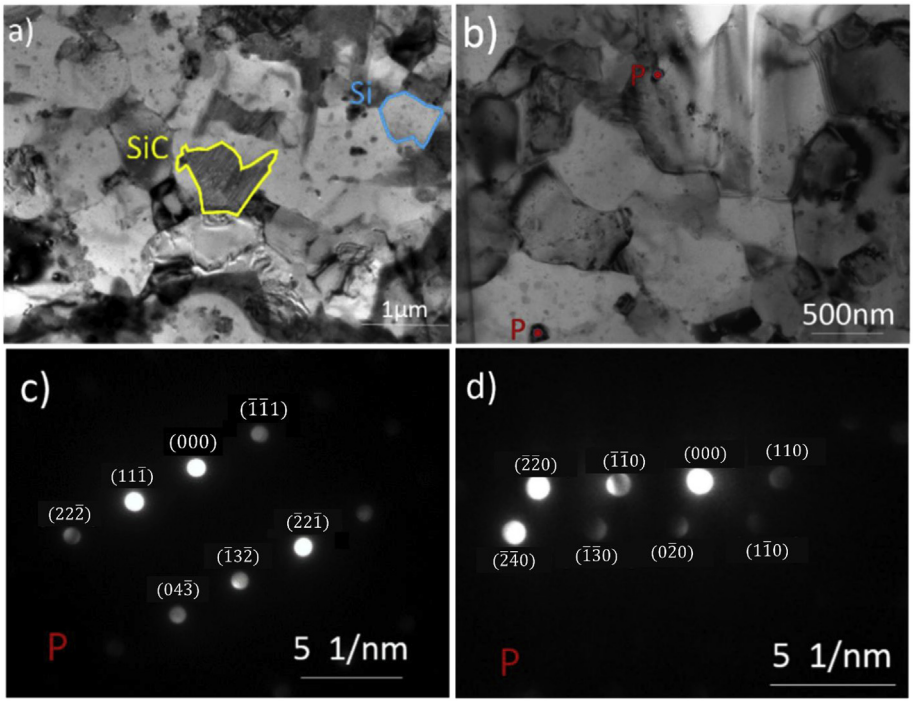

Fig. 13. TEM characterization of the recycled Si mixture with 10 at.% P substitution. a) Morphologies of Si and SiC grains. b) The morphologies of P precipitates, which are clarified by the diffraction patterns in c) and d). The reflections in c) and d) are compared with the calculated diffraction patterns of P crystals (space group 64) assuming a [134] and [001] zone axis, respectively.

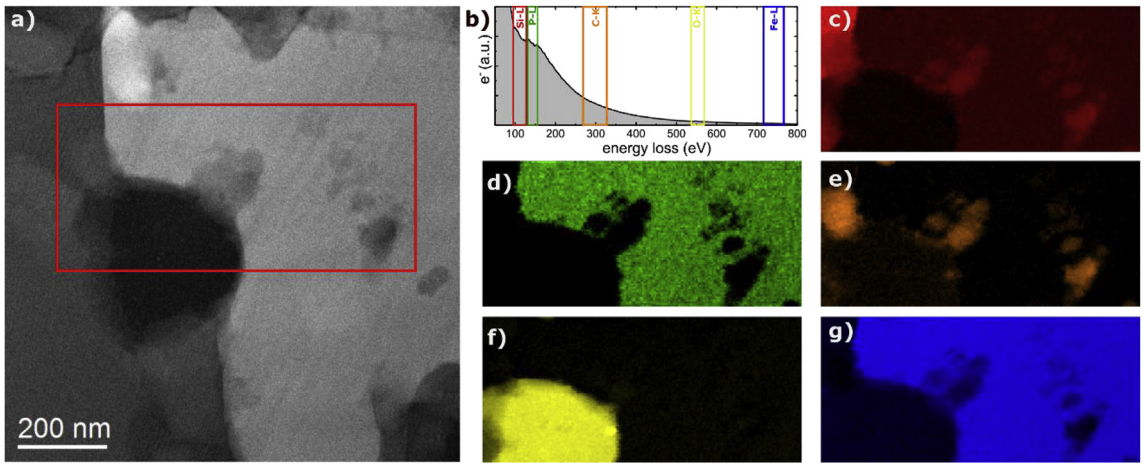

Fig. 14. High-resolution scanning transmission electron microscopy (HR-STEM) and EELS measurements of the Si slurry sample with 10 at.% P. a) Annular dark field image with marked area for local EELS measurements. b) Overview EEL spectra with marked element edges used for elemental mapping. c)-g) Color-coded elemental maps of Si-L, P-L, C-K, O-K, and Fe-L, respectively.

that of Si [193]. Therefore, we assume that all of the ionization of P occurs only in the Si grains and that no dopant enters the SiC lattice. To study the influence of the dopant atoms on the thermoelectric properties, we selected P amounts of 0.1 at.%, 0.2 at.%, 1 at.%, 2 at.%, 3 at.%, 6 at.%, 8 at.%, and 10 at.%. As a reference, we also synthesized a pure Si sample with 2 at.% P substitution. The experimental details can be found in the supplementary information.

Fig. 12 shows the X-ray diffraction (XRD) patterns of all of the compositions after sintering, where obvious peaks of Si and SiC are present. Also, increased peaks of SiP are evident with higher concentration of P, suggesting the limited solubility of P in Si. There are also several minor peaks that cannot be identified, possibly belonging to some metallic compounds. TEM results, as shown in Fig. 13a, indicate that Si and SiC have grain sizes of ~500–800 nm. Moreover, a considerable amount of precipitates is also observed. As shown in Fig. 13b, these precipitates typically possess sizes of 10–50 nm. Electron diffraction patterns of these precipitates suggest that they are phosphorous crystals (space group 64, a = 0.331 nm; b = 1.048 nm; c = 0.436 nm), as shown in Fig. 13c and d with comparisons to the calculated diffraction patterns of P crystals assuming a [134] and [001] zone axis, respectively. Local electron energy loss spectroscopy (EELS, Fig. 14a and b) investigations of the P-L edge show clearly the P incorporation into the Si matrix (Figs. 3.4c-d). P seems to be less present in regions with higher C concentration (Fig. 14e), which is in agreement with the reduced solubility of P in SiC. Additionally, the presence of O and Fe (Fig. 14f and g) in the Si matrix lead to more complex compounds and might explain the unknown minor peaks in the XRD patterns.

We observe an increasing trend of sample density with respect to the phosphorus content (see Table S2 in the supplementary information). This is probably due to the sintering process: the conductivity is lower in the less-doped samples, and therefore less current passes through the powder, which is unfavorable for obtaining high density samples. A low density is usually disadvantageous for TE performance since the electrical conductivity is significantly reduced.

In Fig. 15, the carrier concentration n_H is plotted against the P content. The carrier density increases from 1.7×10^{18} cm^{-3} to 2.1×10^{20} cm^{-3} with 0.1 at.% and 2 at.% P substitution, respectively. By increasing the phosphorus concentration to above 2%, the charge carrier density changes little. By subtracting the SiC volume, the saturation carrier density in Si reaches ~2.53×10^{20} cm^{-3}, which is lower than the saturation value of ~3.5×10^{20} cm^{-3} in Si as reported by Zhu et al. [116]. The decreased solubility of P in our compounds possibly originates from the compressively strained Si lattices due to its mixture with SiC.

The temperature-dependent TE performances of the compositions in this study are shown in Fig. 16. Upon the addition of P, electrical resistivity decreases dramatically, as shown in Fig. 16a. Additionally, with 0.1% doping, the resistivity decreases with higher temperature; on the other hand, the resistivity increases with temperature when the dopant concentration is higher. The resistivity variations suggest a gradual transition from a semiconductor to metallic behavior upon P doping. In addition, the resistivity of the 2 at.% P-doped silicon is much lower than that of the recycled Si. This is due to the presence of SiC that scatters charge carriers, as well as the decreased carrier concentration (Fig. 15) in comparison to pure Si. It should be noted that at temperatures higher than 1000 K, the resistivity drops again for these highly doped compositions. This is because of the bipolar effects where the intrinsic excitation of electron-hole pairs enhances the overall charge carrier concentrations in these compounds.

Fig. 16b shows the temperature-dependent Seebeck coefficients.

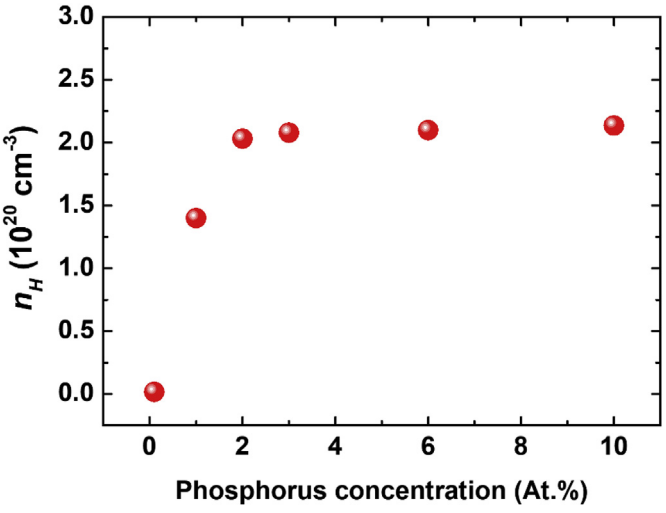

Fig. 15. Carrier concentration with respect to the phosphorus concentration.

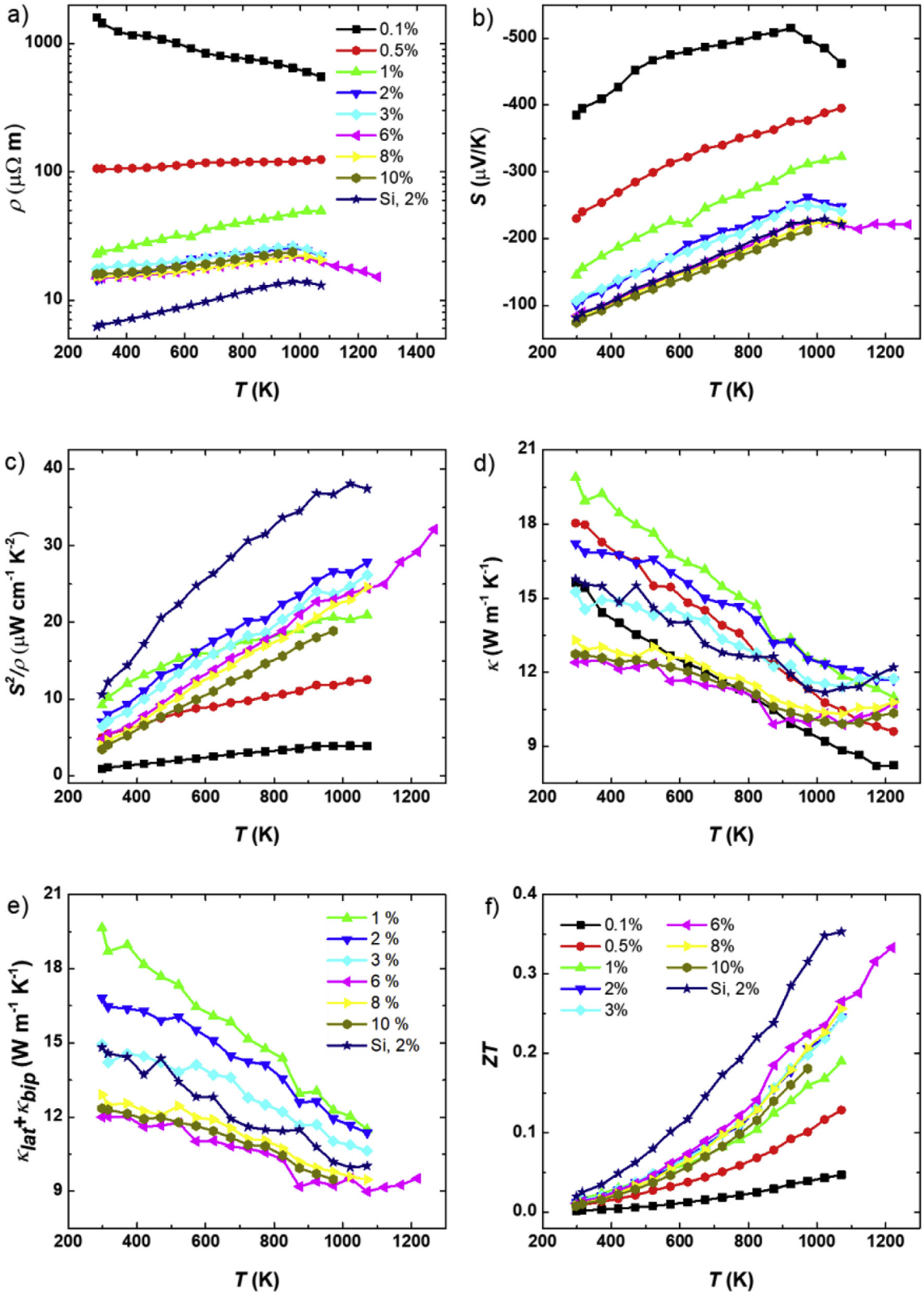

Fig. 16. Temperature-dependent thermoelectric properties, a) electrical resistivity, b) the Seebeck coefficient, c) power factor, d) thermal conductivity, e) lattice plus bipolar thermal conductivity, and f) *zT*, of recycled Si with 0.1 at.%, 0.5 at.%, 1 at.%, 2 at.%, 3 at.%, 6 at.%, 8 at.%, and 10 at.% P substitution at Si. The TE properties of 2 at.% P-substituted Si is also plotted.

As expected, the Seebeck coefficients are lower with higher amounts of carrier density. This is in good agreement with the single parabolic band assumption [194]. The combined electrical resistivity and Seebeck coefficient yields the *PF*, as shown in Fig. 16c. The peak *PF* value at 1073 K reaches ~28 $\mu W\,cm^{-1}\,K^{-2}$ for the recycled Si with 2 at.% P substitution, compared to the *PF* of ~37 $\mu W\,cm^{-1}\,K^{-2}$ for the 2 at.% P-doped reference Si. By further increasing the temperature to 1273 K, we obtain a higher *PF* of ~32 $\mu W\,cm^{-1}\,K^{-2}$ with 6 at.% P substitution, which is comparable to doped SiGe alloys [85].

Fig. 16d shows the thermal conductivity. In general, the value of κ decreases with higher concentration of P. It should be noted that the samples with 0.1% and 0.5% doping have abnormally low κ. This is because of their relatively low densities, as shown in Table S2 in the supplementary information. By subtracting the electronic thermal conductivity (κ_e) using the Wiedmann-Franz law $\kappa_e = LT/\rho$, where L is the Lorenz number determined from the single parabolic band (SPB) model with an approximate equation [195], $L = 1.5 + exp\left(-\frac{|S|}{116}\right)$, we plot the sum of lattice and bipolar thermal conductivity ($\kappa_L+\kappa_{bip}$) in Fig. 16e. Clearly, the reduction of κ originates from the decreased κ_L, with the possible mechanism being an enhanced electron-phonon interaction, which has been widely proven in Si [95,106]. Finally, we obtain a peak *zT* value of ~0.33 in recycled Si with 6 at.% P substitution at 1273 K, as shown in Fig. 16f. The obtained peak *zT* is comparable to that of Si with 2 At.% P doping. Considering the high abundance of Si available from recycled sawing wastes as well as the industrial exigency to turn these "waste" products profitable, we conclude that the recycled Si is an applicable TE material.

4. Summary and outlook

Despite the recently reported ultrahigh *zT* values exceeding 2 in a variety of materials such as GeTe, SnSe, PbTe, *etc.*, the use of environmentally unfavorable elements in these materials such as Te, Se, Pb, *etc.* that are scarce, expensive, toxic, or unstable impedes their large-scale applicability. Here we revisited the experimental TE properties of a variety of Si-related materials as potential candidates to overcome these disadvantages, such as SiGe alloy, nano-bulk structured Si, Si nanowire arrays, *etc*. Due to the excellent electronic transport properties, we highlight the potential of Si as a promising TE material for applications, provided that a great reduction of the thermal conductivity can be achieved. Approaches such as nano-bulk structuring and large area nanowire arrays show some promising advances and deserve further investigation, such as on controllable growth of grain sizes and wire diameters. Ultimate confinement of crystalline size is desired for impeding phonon transport, which might be realized by the emerging technique of flash sintering that is capable of sintering materials in just several seconds at a lower temperature, consequently greatly suppressing the grain growth. Additionally, hybrid structures such as the amorphous-crystalline-core-shell silicon thin films also demonstrate a thermal conductivity that is even lower than the amorphous limit [196], without hindering the electron transport. Therefore higher TE performance is expected upon successfully transferring such structures into bulk silicon.

We also studied the TE properties of Si recycled from sawing waste as a potential approach to translate these industrial wastes into profits. A peak *zT* of ~0.33 and a peak *PF* of ~32 $\mu W\,cm^{-1}\,K^{-2}$ were obtained through heavy P doping. The obtained *PF* is comparable to the n-type SiGe alloys that have been used in modules for power generation applications. We suggest the large-scale applicability of recycled Si due to its high chemical stability, decent electrical properties, high abundance, and especially low material cost.

Conflicts of interest

The authors declare no conflict of interests.

Acknowledgement

The work performed at the University of Houston is funded by the U.S. Department of Energy under Grant DE-SC0010831.

Appendix A. Supplementary data

Supplementary data to this article can be found online at https://doi.org/10.1016/j.jmat.2018.11.004.

References

[1] Tchanche BF, Lambrinos G, Frangoudakis A, Papadakis G. Low-grade heat conversion into power using organic Rankine cycles – a review of various applications. Renew Sustain Energy Rev 2011;15(8):3963–79.
[2] Vélez F, Segovia JJ, Martín MC, Antolín G, Chejne F, Quijano A. A technical, economical and market review of organic Rankine cycles for the conversion of low-grade heat for power generation. Renew Sustain Energy Rev 2012;16(6):4175–89.
[3] Hu R, Cola BA, Haram N, Barisci JN, Lee S, Stoughton S, et al. Harvesting waste thermal energy using a carbon-nanotube-based thermo-electrochemical cell. Nano Lett 2010;10(3):838–46.
[4] Lee SW, Yang Y, Lee H-W, Ghasemi H, Kraemer D, Chen G, et al. An electrochemical system for efficiently harvesting low-grade heat energy. Nat Commun 2014;5.
[5] He R, Schierning G, Nielsch K. Thermoelectric devices: a review of devices, architectures, and contact optimization. Adv Mater Technol 2017:1700256.
[6] Liu Z, Mao J, Liu T-H, Chen G, Ren Z. Nano-microstructural control of phonon engineering for thermoelectric energy harvesting. MRS Bull 2018;43(03):181–6.
[7] He R, Zhu H, Sun J, Mao J, Reith H, Chen S, et al. Improved thermoelectric performance of n-type half-Heusler MCo 1-x Ni x Sb (M = Hf, Zr). Mater Today Phys 2017;1:24–30.
[8] Poudel B, Hao Q, Ma Y, Lan Y, Minnich A, Yu B, et al. High-thermoelectric performance of nanostructured bismuth antimony telluride bulk alloys. Science 2008;320(5876):634–8.
[9] Ma J, Delaire O, May AF, Carlton CE, McGuire MA, VanBebber LH, et al. Glass-like phonon scattering from a spontaneous nanostructure in AgSbTe2. Nat Nanotechnol 2013;8(6):445–51.
[10] Xu J, Li H, Du B, Tang X, Zhang Q, Uher C. High thermoelectric figure of merit and nanostructuring in bulk AgSbTe2. J Mater Chem 2010;20(29):6138.
[11] Pei Y, Shi X, LaLonde A, Wang H, Chen L, Snyder GJ. Convergence of electronic bands for high performance bulk thermoelectrics. Nature 2011;473(7345):66–9.
[12] Heremans JP, Wiendlocha B, Chamoire AM. Resonant levels in bulk thermoelectric semiconductors. Energy Environ Sci 2012;5(2):5510–30.
[13] Liu W, Tan X, Yin K, Liu H, Tang X, Shi J, et al. Convergence of conduction bands as a means of enhancing thermoelectric performance ofn-Type-Mg2Si1−xSnxSolid solutions. Phys Rev Lett 2012;108(16).
[14] He R, Kraemer D, Mao J, Zeng L, Jie Q, Lan Y, et al. Achieving high power factor and output power density in p-type half-Heuslers Nb1-xTixFeSb. Proc Natl Acad Sci Unit States Am 2016;113(48):13576–81.
[15] Shuai J, Mao J, Song S, Zhu Q, Sun J, Wang Y, et al. Tuning the Carrier scattering mechanism to effectively improve the thermoelectric properties. Energy Environ Sci 2017;10(3):799–807.
[16] Ren W, Zhu H, Zhu Q, Saparamadu U, He R, Liu Z, et al. Ultrahigh power factor in thermoelectric system Nb0.95M0.05FeSb (M = Hf, Zr, and Ti). Adv. Sci. 2018:1800278.
[17] Hu L, Wu H, Zhu T, Fu C, He J, Ying P, et al. Tuning multiscale microstructures to enhance thermoelectric performance of n-type bismuth-telluride-based solid solutions. Adv. Energy Mater. 2015;5(17):1500411.
[18] Hu L-P, Zhu T-J, Wang Y-G, Xie H-H, Xu Z-J, Zhao X-B. Shifting up the optimum figure of merit of p-type bismuth telluride-based thermoelectric materials for power generation by suppressing intrinsic conduction. NPG Asia Mater 2014;6(2). e88-e88.
[19] Liu Y, Zhang Y, Ortega S, Ibáñez M, Lim KH, Grau-Carbonell A, et al. Crystallographically textured nanomaterials produced from the liquid phase sintering of BixSb2−xte3 nanocrystal building blocks. Nano Lett 2018;18(4):2557–63.
[20] Yan X, Poudel B, Ma Y, Liu WS, Joshi G, Wang H, et al. Experimental studies

on anisotropic thermoelectric properties and structures of n-type Bi2Te2.7Se0.3. Nano Lett 2010;10(9):3373–8.
[21] Wu Y, Zhai R, Zhu T, Zhao X. Enhancing room temperature thermoelectric performance of n -type polycrystalline bismuth-telluride-based alloys via Ag doping and hot deformation. Mater Today Phys 2017;2:62–8.
[22] Qin H, Liu Y, Zhang Z, Wang Y, Cao J, Cai W, et al. Improved thermoelectric performance of p-type Bi0.5Sb1.5Te3 through Mn doping at elevated temperature. Mater Today Phys 2018;6:31–7.
[23] Zong P-a, Hanus R, Dylla M, Tang Y, Liao J, Zhang Q, et al. Skutterudite with graphene-modified grain-boundary complexion enhances zT enabling high-efficiency thermoelectric device. Energy Environ Sci 2017;10(1):183–91.
[24] Meng X, Liu Z, Cui B, Qin D, Geng H, Cai W, et al. Grain boundary engineering for achieving high thermoelectric performance in n-type skutterudites. Advanced Energy Materials 2017;7(13):1602582.
[25] Ren W, Geng H, Zhang L, Liu X, He T, Feng J. Simultaneous blocking of minority Carrier and high energy phonon in p-type skutterudites. Nanomater Energy 2018;46:249–56.
[26] Moure A, Rull-Bravo M, Abad B, Del Campo A, Rojo MM, Aguirre MH, et al. Thermoelectric Skutterudite/oxide nanocomposites: effective decoupling of electrical and thermal conductivity by functional interfaces. Nanomater Energy 2017;31:393–402.
[27] Zhao W, Liu Z, Sun Z, Zhang Q, Wei P, Mu X, et al. Superparamagnetic enhancement of thermoelectric performance. Nature 2017;549(7671):247–51.
[28] Rogl G, Rogl P. How nanoparticles can change the figure of merit, ZT, and mechanical properties of skutterudites. Mater Today Phys 2017;3:48–69.
[29] Heremans JP, Jovovic V, Toberer ES, Saramat A, Kurosaki K, Charoenphakdee A, et al. Enhancement of thermoelectric efficiency in PbTe by distortion of the electronic density of states. Science 2008;321(5888):554–7.
[30] Jaworski CM, Nielsen MD, Wang H, Girard SN, Cai W, Porter WD, et al. Valence-band structure of highly efficient p-type thermoelectric PbTe-PbS alloys. Phys Rev B 2013;87(4).
[31] Zhang Q, Liao B, Lan Y, Lukas K, Liu W, Esfarjani K, et al. High thermoelectric performance by resonant dopant indium in nanostructured SnTe. Proc Natl Acad Sci Unit States Am 2013;110(33):13261–6.
[32] Li W, Wu Y, Lin S, Chen Z, Li J, Zhang X, et al. Advances in environment-friendly SnTe thermoelectrics. ACS Energy Letters 2017;2(10):2349–55.
[33] Li J, Zhang X, Chen Z, Lin S, Li W, Shen J, et al. Low-symmetry rhombohedral GeTe thermoelectrics. Joule; 2018.
[34] Zhang Q, Chere EK, McEnaney K, Yao M, Cao F, Ni Y, et al. Enhancement of thermoelectric performance of n-type PbSe by Cr doping with optimized Carrier concentration. Advanced Energy Materials 2015;5(8):1401977.
[35] Zhao L-D, Lo S-H, Zhang Y, Sun H, Tan G, Uher C, et al. Ultralow thermal conductivity and high thermoelectric figure of merit in SnSe crystals. Nature 2014;508(7496):373–7.
[36] Liu Z, Sun J, Mao J, Zhu H, Ren W, Zhou J, et al. Phase-transition temperature suppression to achieve cubic GeTe and high thermoelectric performance by Bi and Mn codoping. Proc Natl Acad Sci Unit States Am 2018;115(21):5332–7.
[37] Bhat DK, Shenoy US. Enhanced thermoelectric performance of bulk tin telluride: synergistic effect of calcium and indium co-doping. Mater Today Phys 2018;4:12–8.
[38] Su CH. Experimental determination of lattice thermal conductivity and Lorenz number as functions of temperature for n-type PbTe. Mater Today Phys 2018;5:58–63.
[39] Wang X, Li X, Zhang Z, Li X, Chen C, Li S, et al. Thermoelectric properties of n-type transition metal-doped PbSe. Mater Today Phys 2018;6:45–52.
[40] Wu Y, Li W, Faghaninia A, Chen Z, Li J, Zhang X, et al. Promising thermoelectric performance in van der Waals layered SnSe2. Mater Today Phys 2017;3:127–36.
[41] Yan X, Joshi G, Liu W, Lan Y, Wang H, Lee S, et al. Enhanced thermoelectric figure of merit of p-type half-Heuslers. Nano Lett 2011;11(2):556–60.
[42] Joshi G, He R, Engber M, Samsonidze G, Pantha T, Dahal E, et al. NbFeSb-based p-type half-Heuslers for power generation applications. Energy Environ Sci 2014;7(12):4070–6.
[43] He R, Kim HS, Lan Y, Wang D, Chen S, Ren Z. Investigating the thermoelectric properties of p-type half-Heusler Hfx(ZrTi)1−xCoSb0.8Sn0.2 by reducing Hf concentration for power generation. RSC Adv 2014;4(110):64711–6.
[44] Huang L, He R, Chen S, Zhang H, Dahal K, Zhou H, et al. A new n-type half-Heusler thermoelectric material NbCoSb. Mater Res Bull 2015;70:773–8.
[45] He R, Huang L, Wang Y, Samsonidze G, Kozinsky B, Zhang Q, et al. Enhanced thermoelectric properties of n-type NbCoSn half-Heusler by improving phase purity. Apl Mater 2016;4(10):104804.
[46] Yu J, Fu C, Liu Y, Xia K, Aydemir U, Chasapis TC, et al. Unique role of refractory Ta alloying in enhancing the figure of merit of NbFeSb thermoelectric materials. Advanced Energy Materials 2018;8(1):1701313.
[47] Fu C, Zhu T, Liu Y, Xie H, Zhao X. Band engineering of high performance p-type FeNbSb based half-Heusler thermoelectric materials for figure of merit zT > 1. Energy Environ Sci 2015;8(1):216–20.
[48] Fu C, Bai S, Liu Y, Tang Y, Chen L, Zhao X, et al. Realizing high figure of merit in heavy-band p-type half-Heusler thermoelectric materials. Nat Commun 2015;6(1).
[49] Xie W, Weidenkaff A, Tang X, Zhang Q, Poon J, Tritt T. Recent advances in nanostructured thermoelectric half-Heusler compounds. Nanomaterials 2012;2(4):379–412.
[50] Gürth M, Rogl G, Romaka VV, Grytsiv A, Bauer E, Rogl P. Thermoelectric high ZT half-Heusler alloys Ti 1−x−y Zr x Hf y NiSn ($0 \le x \le 1$; $0 \le y \le 1$). Acta Mater 2016;104:210–22.
[51] Rausch E, Balke B, Ouardi S, Felser C. Enhanced thermoelectric performance in the p-type half-Heusler (Ti/Zr/Hf)CoSb0.8Sn0.2 system via phase separation. Phys Chem Chem Phys 2014;16(46):25258–62.
[52] Mao J, Kim HS, Shuai J, Liu Z, He R, Saparamadu U, et al. Thermoelectric properties of materials near the band crossing line in Mg 2 Sn–Mg 2 Ge–Mg 2 Si system. Acta Mater 2016;103:633–42.
[53] Liu W, Kim HS, Chen S, Jie Q, Lv B, Yao M, et al. n-type thermoelectric material Mg2Sn0.75Ge0.25 for high power generation. Proc Natl Acad Sci Unit States Am 2015;112(11):3269–74.
[54] Liu X, Zhu T, Wang H, Hu L, Xie H, Jiang G, et al. Low electron scattering potentials in high performance Mg2Si0.45Sn0.55 Based thermoelectric solid solutions with band convergence. Advanced Energy Materials 2013;3(9):1238–44.
[55] de Boor J, Saparamadu U, Mao J, Dahal K, Müller E, Ren Z. Thermoelectric performance of Li doped, p-type Mg 2 (Ge,Sn) and comparison with Mg 2 (Si,Sn). Acta Mater 2016;120:273–80.
[56] Shuai J, Geng H, Lan Y, Zhu Z, Wang C, Liu Z, et al. Higher thermoelectric performance of Zintl phases (Eu0.5Yb0.5)1−xCaxMg2Bi2by band engineering and strain fluctuation. Proc Natl Acad Sci Unit States Am 2016;113(29):E4125–32.
[57] Tamaki H, Sato HK, Kanno T. Isotropic conduction network and defect chemistry in Mg3+δsb2-based layered Zintl compounds with high thermoelectric performance. Adv Mater 2016;28(46):10182–7.
[58] Mao J, Shuai J, Song S, Wu Y, Dally R, Zhou J, et al. Manipulation of ionized impurity scattering for achieving high thermoelectric performance in n-type Mg3Sb2-based materials. Proc Natl Acad Sci Unit States Am 2017;114(40):10548–53.
[59] Toberer ES, Cox CA, Brown SR, Ikeda T, May AF, Kauzlarich SM, et al. Traversing the metal-insulator transition in a Zintl phase: rational enhancement of thermoelectric efficiency in Yb14Mn1−xAlxSb11. Adv Funct Mater 2008;18(18):2795–800.
[60] Song S, Mao J, Shuai J, Zhu H, Ren Z, Saparamadu U, et al. Study on anisotropy of n-type Mg3Sb2-based thermoelectric materials. Appl Phys Lett 2018;112(9), 092103.
[61] Mao J, Wu Y, Song S, Shuai J, Liu Z, Pei Y, et al. Anomalous electrical conductivity of n-type Te-doped Mg3.2Sb1.5Bi0.5. Mater Today Phys 2017;3:1–6.
[62] Shuai J, Mao J, Song S, Zhang Q, Chen G, Ren Z. Recent progress and future challenges on thermoelectric Zintl materials. Mater Today Phys 2017;1:74–95.
[63] Sun J, Shuai J, Ren Z, Singh DJ. Computational modelling of the thermoelectric properties of p -type Zintl compound CaMg 2 Bi 2. Mater Today Phys 2017;2:40–5.
[64] Liu Z, Mao J, Peng S, Zhou B, Gao W, Sui J, et al. Tellurium doped n -type Zintl Zr 3 Ni 3 Sb 4 thermoelectric materials: balance between Carrier-scattering mechanism and bipolar effect. Mater Today Phys 2017;2:54–61.
[65] Song Q, Liu T-H, Zhou J, Ding Z, Chen G. Ab initio study of electron mean free paths and thermoelectric properties of lead telluride. Mater Today Phys 2017;2:69–77.
[66] Zhao H, Sui J, Tang Z, Lan Y, Jie Q, Kraemer D, et al. High thermoelectric performance of MgAgSb-based materials. Nanomater Energy 2014;7:97–103.
[67] Shuai J, Kim HS, Lan Y, Chen S, Liu Y, Zhao H, et al. Study on thermoelectric performance by Na doping in nanostructured Mg 1-x Na x Ag 0.97 Sb 0.99. Nanomater Energy 2015;11:640–6.
[68] Liu Z, Wang Y, Gao W, Mao J, Geng H, Shuai J, et al. The influence of doping sites on achieving higher thermoelectric performance for nanostructured α-MgAgSb. Nanomater Energy 2017;31:194–200.
[69] Liu Z, Wang Y, Mao J, Geng H, Shuai J, Wang Y, et al. Lithium doping to enhance thermoelectric performance of MgAgSb with weak electron-phonon coupling. Advanced Energy Materials 2016;6(7):1502269.
[70] Sui J, Shuai J, Lan Y, Liu Y, He R, Wang D, et al. Effect of Cu concentration on thermoelectric properties of nanostructured p -type MgAg 0.97− x Cu x Sb 0.99. Acta Mater 2015;87:266–72.
[71] Ying P, Liu X, Fu C, Yue X, Xie H, Zhao X, et al. High performance α-MgAgSb thermoelectric materials for low temperature power generation. Chem Mater 2015;27(3):909–13.
[72] Kraemer D, Sui J, McEnaney K, Zhao H, Jie Q, Ren ZF, et al. High thermoelectric conversion efficiency of MgAgSb-based material with hot-pressed contacts. Energy Environ Sci 2015;8(4):1299–308.
[73] Lee JK, Oh M-W, Ryu B, Lee JE, Kim B-S, Min B-K, et al. Enhanced thermoelectric properties of AgSbTe2 obtained by controlling heterophases with Ce doping. Sci Rep 2017;7(1).
[74] Wang H, Li J-F, Zou M, Sui T. Synthesis and transport property of AgSbTe2 as a promising thermoelectric compound. Appl Phys Lett 2008;93(20):202106.

[75] Zhao K, Qiu P, Song Q, Blichfeld AB, Eikeland E, Ren D, et al. Ultrahigh thermoelectric performance in Cu 2–y Se 0.5 S 0.5 liquid-like materials. Mater Today Phys 2017;1:14–23.
[76] Kang SD, Pöhls J-H, Aydemir U, Qiu P, Stoumpos CC, Hanus R, et al. Enhanced stability and thermoelectric figure-of-merit in copper selenide by lithium doping. Mater Today Phys 2017;1:7–13.
[77] Jiang B, Qiu P, Chen H, Huang J, Mao T, Wang Y, et al. Entropy optimized phase transitions and improved thermoelectric performance in n-type liquid-like Ag 9 GaSe 6 materials. Mater Today Phys 2018;5:20–8.
[78] Lin S, Li W, Bu Z, Gao B, Li J, Pei Y. Thermoelectric properties of Ag9GaS6 with ultralow lattice thermal conductivity. Mater Today Phys 2018;6:60–7.
[79] Zhu GH, Lee H, Lan YC, Wang XW, Joshi G, Wang DZ, et al. Increased phonon scattering by nanograins and point defects in nanostructured silicon with a low concentration of germanium. Phys Rev Lett 2009;102(19).
[80] Glassbrenner CJ, Slack GA. Thermal conductivity of silicon and germanium from 3°K to the melting point. Phys Rev 1964;134(4A):A1058–69.
[81] Mao J, Wang Y, Kim HS, Liu Z, Saparamadu U, Tian F, et al. High thermoelectric power factor in Cu–Ni alloy originate from potential barrier scattering of twin boundaries. Nanomater Energy 2015;17:279–89.
[82] Chen S, Lukas KC, Liu W, Opeil CP, Chen G, Ren Z. Effect of Hf concentration on thermoelectric properties of nanostructured N-type half-Heusler materials HfxZr1-xNiSn0.99Sb0.01. Advanced Energy Materials 2013;3(9):1210–4.
[83] Zhang J, Wu D, He D, Feng D, Yin M, Qin X, et al. Extraordinary thermoelectric performance realized in n-type PbTe through multiphase nanostructure engineering. Adv Mater 2017;29(39):1703148.
[84] Duong AT, Nguyen VQ, Duvjir G, Duong VT, Kwon S, Song JY, et al. Achieving ZT=2.2 with Bi-doped n-type SnSe single crystals. Nat Commun 2016;7:13713.
[85] Wang XW, Lee H, Lan YC, Zhu GH, Joshi G, Wang DZ, et al. Enhanced thermoelectric figure of merit in nanostructured n-type silicon germanium bulk alloy. Appl Phys Lett 2008;93(19):193121–3.
[86] Tan G, Shi F, Hao S, Zhao L-D, Chi H, Zhang X, et al. Non-equilibrium processing leads to record high thermoelectric figure of merit in PbTe–SrTe. Nat Commun 2016;7:12167.
[87] Joshi G, Lee H, Lan Y, Wang X, Zhu G, Wang D, et al. Enhanced thermoelectric figure-of-merit in nanostructured p-type silicon germanium bulk alloys. Nano Lett 2008;8(12):4670–4.
[88] Hicks LD, Dresselhaus MS. Effect of quantum-well structures on the thermoelectric figure of merit. Phys Rev B 1993;47(19):12727.
[89] Hicks LD, Dresselhaus MS. Thermoelectric figure of merit of a one-dimensional conductor. Phys Rev B 1993;47(24):16631.
[90] Dresselhaus MS, Chen G, Tang MY, Yang RG, Lee H, Wang DZ, et al. New directions for low-dimensional thermoelectric materials. Adv Math 2007;19(8):1043–53.
[91] Yusufu A, Kurosaki K, Miyazaki Y, Ishimaru M, Kosuga A, Ohishi Y, et al. Bottom-up nanostructured bulk silicon: a practical high-efficiency thermoelectric material. Nanoscale 2014;6(22):13921–7.
[92] Hochbaum AI, Chen R, Delgado RD, Liang W, Garnett EC, Najarian M, et al. Enhanced thermoelectric performance of rough silicon nanowires. Nature 2008;451(7175):163–7.
[93] Boukai AI, Bunimovich Y, Tahir-Kheli J, Yu J-K, Goddard Iii WA, Heath JR. Silicon nanowires as efficient thermoelectric materials. Nature 2008;451(7175):168–71.
[94] Bux SK, Blair RG, Gogna PK, Lee H, Chen G, Dresselhaus MS, et al. Nanostructured bulk silicon as an effective thermoelectric material. Adv Funct Mater 2009;19(15):2445–52.
[95] Dismukes JP, Ekstrom L, Steigmeier EF, Kudman I, Beers DS. Thermal and electrical properties of heavily doped Ge-Si alloys up to 1300°K. J Appl Phys 1964;35(10):2899–907.
[96] Abeles B, Beers DS, Cody GD, Dismukes JP. Thermal conductivity of Ge-Si alloys at high temperatures. Phys Rev 1962;125(1):44–6.
[97] Steele MC, Rosi FD. Thermal conductivity and thermoelectric power of germanium-silicon alloys. J Appl Phys 1958;29(11):1517–20.
[98] Rowe DM, Bunce RW. The thermoelectric properties of heavily doped hot-pressed germanium-silicon alloys. J Phys Appl Phys 1969;2(11):1497–502.
[99] Lefever RA, McVay GL, Baughman RJ. Preparation of hot-pressed silicon-germanium ingots: Part III - vacuum hot pressing. Mater Res Bull 1974;9(7):863–72.
[100] McVay GL, Lefever RA, Baughman RJ. Preparation of hot-pressed silicon-germanium ingots: Part II - reduction of chill cast material. Mater Res Bull 1974;9(6):735–44.
[101] Rowe DM. Electrical properties of hot-pressed germanium-silicon-boron alloys. J Phys Appl Phys 1975;8(9):1092–103.
[102] Rowe DM, Shukla VS, Savvides N. Phonon scattering at grain boundaries in heavily doped fine-grained silicon–germanium alloys. Nature 1981;290(5809):765–6.
[103] Vining CB, Laskow W, Hanson JO, Van der Beck RR, Gorsuch PD. Thermoelectric properties of pressure-sintered Si0.8Ge0.2 thermoelectric alloys. J Appl Phys 1991;69(8):4333–40.
[104] Klemens PG. Thermal resistance due to point defects at high temperatures. Phys Rev 1960;119(2):507–9.
[105] Abeles B. Lattice thermal conductivity of disordered semiconductor alloys at high temperatures. Phys Rev 1963;131(5):1906–11.
[106] Liao B, Qiu B, Zhou J, Huberman S, Esfarjani K, Chen G. Significant reduction of lattice thermal conductivity by the electron-phonon interaction in silicon with high Carrier concentrations: a first-principles study. Phys Rev Lett 2015;114(11).
[107] Bhandari CM, Rowe DM. Silicon–germanium alloys as high-temperature thermoelectric materials. Contemp Phys 2006;21(3):219–42.
[108] Slack GA, Hussain MA. The maximum possible conversion efficiency of silicon-germanium thermoelectric generators. J Appl Phys 1991;70(5):2694–718.
[109] Abrikosov NK, Zemskov VS, Iordanishvili EK, Petrov AV, Rozhdestvenskaya VV. Thermoelectric properties of silicon-germanium-boron alloys. Sov. Phys. Semiconductors 1969;2(12):1468–73.
[110] Yusufu A, Kurosaki K, Miyazaki Y, Ishimaru M, Kosuga A, Ohishi Y, et al. Role of nanoscale precipitates for enhancement of thermoelectric properties of heavily P-doped Si-Ge alloys. Mater Trans 2016;57(7):1070–5.
[111] Dismukes JP, Ekstrom L. Homogeneous solidification of Ge-Si alloys. Trans. Metall. Soc. AIME 1965;233(4):672. & %@ 0543-5722.
[112] Savvides N, Goldsmid HJ. Hot-press sintering of Ge-Si alloys. J Mater Sci 1980;15(3):594–600.
[113] Cahill DG, Pohl RO. Heat flow and lattice vibrations in glasses. Solid State Commun 1989;70(10):927–30.
[114] Goldsmid HJ, Penn AW. Boundary scattering of phonons in solid solutions. Phys Lett 1968;27(8):523–4.
[115] Nakajima Y, Takeda S, Nagao T, Hasegawa S, Tong X. Surface electrical conduction due to Carrier doping into a surface-state band on Si(111)-3×3-Ag. Phys Rev B 1997;56(11):6782–7.
[116] Zhu T, Yu G, Xu J, Wu H, Fu C, Liu X, et al. The role of electron-phonon interaction in heavily doped fine-grained bulk silicons as thermoelectric materials. Adv. Electron. Mater. 2016;2(8):1600171.
[117] Hao Q, Zhu G, Joshi G, Wang X, Minnich A, Ren Z, et al. Theoretical studies on the thermoelectric figure of merit of nanograined bulk silicon. Appl Phys Lett 2010;97(6). 063109-063103.
[118] Claudio T, Stein N, Stroppa DG, Klobes B, Koza MM, Kudejova P, et al. Nanocrystalline silicon: lattice dynamics and enhanced thermoelectric properties. Phys Chem Chem Phys 2014;16(47):25701–9.
[119] Kessler V, Gautam D, Hülser T, Spree M, Theissmann R, Winterer M, et al. Thermoelectric properties of nanocrystalline silicon from a scaled-up synthesis plant. Adv Eng Mater 2013;15(5):379–85.
[120] Schierning G, Theissmann R, Stein N, Petermann N, Becker A, Engenhorst M, et al. Role of oxygen on microstructure and thermoelectric properties of silicon nanocomposites. J Appl Phys 2011;110(11):113515–9.
[121] Schierning G, Stoetzel J, Chavez R, Kessler V, Hall J, Schmechel R, et al. Silicon-based nanocomposites for thermoelectric application. Phys Status Solidi 2016;213(3):497–514.
[122] Petermann N, Stein N, Schierning G, Theissmann R, Stoib B, Brandt MS, et al. Plasma synthesis of nanostructures for improved thermoelectric properties. J Phys Appl Phys 2011;44(17):174034.
[123] Hülser T, Schnurre SM, Wiggers H, Schulz C. Gas-phase synthesis of nanoscale silicon as an economical route towards sustainable energy technology. KONA Powder Particle J 2011;29(0):191–207.
[124] Dingle R, Störmer HL, Gossard AC, Wiegmann W. Electron mobilities in modulation-doped semiconductor heterojunction superlattices. Appl Phys Lett 1978;33(7):665–7.
[125] Zebarjadi M, Joshi G, Zhu G, Yu B, Minnich A, Lan Y, et al. Power factor enhancement by modulation doping in bulk nanocomposites. Nano Lett 2011;11(6):2225–30.
[126] Yu B, Zebarjadi M, Wang H, Lukas K, Wang H, Wang D, et al. Enhancement of thermoelectric properties by modulation-doping in silicon germanium alloy nanocomposites. Nano Lett 2012;12(4):2077–82.
[127] Hicks LD, Harman TC, Sun X, Dresselhaus MS. Experimental study of the effect of quantum-well structures on the thermoelectric figure of merit. Phys Rev B 1996;53(16):R10493–6.
[128] Koga T, Cronin SB, Dresselhaus MS, Liu JL, Wang KL. Experimental proof-of-principle investigation of enhanced Z3DT in (001) oriented Si/Ge superlattices. Appl Phys Lett 2000;77(10):1490–2.
[129] Ravich YI, Efimova BA, Tamarchenko VI. Scattering of current carriers and transport phenomena in lead chalcogenides II. Experiment. Phys Status Solidi 1971;43(2):453–69.
[130] Hicks LD, Harman TC, Dresselhaus MS. Use of quantum-well superlattices to obtain a high figure of merit from nonconventional thermoelectric materials. Appl Phys Lett 1993;63(23):3230–2.
[131] Slack GA. The Thermal Conductivity of Nonmetallic Crystals 1979;34:1–71.
[132] Li D, Wu Y, Kim P, Shi L, Yang P, Majumdar A. Thermal conductivity of individual silicon nanowires. Appl Phys Lett 2003;83(14):2934–6.
[133] Shakouri A. Recent developments in semiconductor thermoelectric physics and materials. Annu Rev Mater Res 2011;41(1):399–431.
[134] Chen R, Hochbaum AI, Murphy P, Moore J, Yang P, Majumdar A. Thermal conductance of thin silicon nanowires. Phys Rev Lett 2008;101(10).
[135] Donadio D, Galli G. Atomistic simulations of heat transport in silicon nanowires. Phys Rev Lett 2009;102(19).
[136] Wang Z, Ni Z, Zhao R, Chen M, Bi K, Chen Y. The effect of surface roughness on lattice thermal conductivity of silicon nanowires. Phys B Condens Matter

2011;406(13):2515–20.
[137] Martin P, Aksamija Z, Pop E, Ravaioli U. Impact of phonon-surface roughness scattering on thermal conductivity of thin Si nanowires. Phys Rev Lett 2009;102(12).
[138] Luisier M. Investigation of thermal transport degradation in rough Si nanowires. J Appl Phys 2011;110(7), 074510.
[139] Chen Y-R, Jeng MS, Chou YW, Yang CC. Molecular dynamics simulation of the thermal conductivities of Si nanowires with various roughnesses. Comput Mater Sci 2011;50(6):1932–6.
[140] Moore AL, Saha SK, Prasher RS, Shi L. Phonon backscattering and thermal conductivity suppression in sawtooth nanowires. Appl Phys Lett 2008;93(8), 083112.
[141] Sadhu J, Sinha S. Room-temperature phonon boundary scattering below the Casimir limit. Phys Rev B 2011;84(11).
[142] Sansoz F. Surface faceting dependence of thermal transport in silicon nanowires. Nano Lett 2011;11(12):5378–82.
[143] Carrete J, Gallego LJ, Varela LM, Mingo N. Surface roughness and thermal conductivity of semiconductor nanowires: going below the Casimir limit. Phys Rev B 2011;84(7).
[144] Lim J, Hippalgaonkar K, Andrews SC, Majumdar A, Yang P. Quantifying surface roughness effects on phonon transport in silicon nanowires. Nano Lett 2012;12(5):2475–82.
[145] Curtin BM, Fang EW, Bowers JE. Highly ordered vertical silicon nanowire array composite thin films for thermoelectric devices. J Electron Mater 2012;41(5):887–94.
[146] Bin X, Khouri W, Fobelets K. Two-sided silicon nanowire array/bulk thermoelectric power generator. IEEE Electron Device Lett 2014;35(5):596–8.
[147] Li Y, Buddharaju K, Tinh BC, Singh N, Lee SJ. Improved vertical silicon nanowire based thermoelectric power generator with polyimide filling. IEEE Electron Device Lett 2012;33(5):715–7.
[148] Abramson AR, Kim WC, Huxtable ST, Yan H, Wu Y, Majumdar A, et al. Fabrication and characterization of a nanowire/polymer-based nanocomposite for a prototype thermoelectric device. J. Microelectromechanical Syst. 2004;13(3):505–13.
[149] Fonseca L, Santos J-D, Roncaglia A, Narducci D, Calaza C, Salleras M, et al. Smart integration of silicon nanowire arrays in all-silicon thermoelectric micro-nanogenerators. Semicond Sci Technol 2016;31(8), 084001.
[150] Tahrim AA, Ahmad A, Ali MSM. Silicon nanowire arrays thermoelectric power harvester. 2017. p. 728–31.
[151] Zhang T, Wu S, Xu J, Zheng R, Cheng G. High thermoelectric figure-of-merits from large-area porous silicon nanowire arrays. Nanomater Energy 2015;13:433–41.
[152] Liu X, Wu X, Ren T. In situ and noncontact measurement of silicon membrane thermal conductivity. Appl Phys Lett 2011;98(17):174104.
[153] Balandin AA. Thermal properties of graphene and nanostructured carbon materials. Nat Mater 2011;10(8):569–81.
[154] Burzo MG, Komarov PL, Raad PE. Influence of the metallic absorption layer on the quality of thermal conductivity measurements by the transient thermo-reflectance method. Microelectron J 2002;33(9):697–703.
[155] Schmidt AJ, Cheaito R, Chiesa M. A frequency-domain thermoreflectance method for the characterization of thermal properties. Rev Sci Instrum 2009;80(9), 094901.
[156] Graebner JE. Measurement of thermal diffusivity by optical excitation and infrared detection of a transient thermal grating. Rev Sci Instrum 1995;66(7):3903–6.
[157] Zhou H, Kropelnicki P, Lee C. Characterization of nanometer-thick polycrystalline silicon with phonon-boundary scattering enhanced thermoelectric properties and its application in infrared sensors. Nanoscale 2015;7(2):532–41.
[158] Valalaki K, Vouroutzis N, Nassiopoulou AG. Significant enhancement of the thermoelectric figure of merit of polycrystalline Si films by reducing grain size. J Phys Appl Phys 2016;49(31):315104.
[159] Wight NM, Acosta E, Vijayaraghavan RK, McNally PJ, Smirnov V, Bennett NS. A universal method for thermal conductivity measurements on micro-/nano-films with and without substrates using micro-Raman spectroscopy. Thermal Sci. Eng. Progress 2017;3:95–101.
[160] Acosta E, Wight NM, Smirnov V, Buckman J, Bennett NS. Hydrogenated nano-/micro-crystalline silicon thin-films for thermoelectrics. J Electron Mater 2018;47(6):3077–84.
[161] Ju YS, Goodson KE. Phonon scattering in silicon films with thickness of order 100 nm. Appl Phys Lett 1999;74(20):3005–7.
[162] Liu W, Asheghi M. Thermal conductivity measurements of ultra-thin single crystal silicon layers. J Heat Tran 2006;128(1):75.
[163] Chávez-Ángel E, Reparaz JS, Gomis-Bresco J, Wagner MR, Cuffe J, Graczykowski B, et al. Reduction of the thermal conductivity in free-standing silicon nano-membranes investigated by non-invasive Raman thermometry. Apl Mater 2014;2(1), 012113.
[164] Strasser M, Aigner R, Lauterbach C, Sturm TF, Franosch M, Wachutka G. Micromachined CMOS thermoelectric generators as on-chip power supply. Sensor Actuator Phys 2004;114(2–3):362–70.
[165] Xie J, Lee C, Wang M-F, Liu Y, Feng H. Characterization of heavily doped polysilicon films for CMOS-MEMS thermoelectric power generators. J Micromech Microeng 2009;19(12):125029.
[166] Bennett NS, Byrne D, Cowley A, Neophytou N. Dislocation loops as a mechanism for thermoelectric power factor enhancement in silicon nanolayers. Appl Phys Lett 2016;109(17):173905.
[167] Perez-Taborda JA, Muñoz Rojo M, Maiz J, Neophytou N, Martin-Gonzalez M. Ultra-low thermal conductivities in large-area Si-Ge nanomeshes for thermoelectric applications. Sci Rep 2016;6(1).
[168] Song D, Chen G. Thermal conductivity of periodic microporous silicon films. Appl Phys Lett 2004;84(5):687–9.
[169] Hopkins PE, Reinke CM, Su MF, Olsson RH, Shaner EA, Leseman ZC, et al. Reduction in the thermal conductivity of single crystalline silicon by phononic crystal patterning. Nano Lett 2011;11(1):107–12.
[170] Yu J-K, Mitrovic S, Tham D, Varghese J, Heath JR. Reduction of thermal conductivity in phononic nanomesh structures. Nat Nanotechnol 2010;5(10):718–21.
[171] Tang J, Wang H-T, Lee DH, Fardy M, Huo Z, Russell TP, et al. Holey silicon as an efficient thermoelectric material. Nano Lett 2010;10(10):4279–83.
[172] Dechaumphai E, Chen R. Thermal transport in phononic crystals: the role of zone folding effect. J Appl Phys 2012;111(7), 073508.
[173] Davis BL, Hussein MI. Nanophononic metamaterial: thermal conductivity reduction by local resonance. Phys Rev Lett 2014;112(5).
[174] Maire J, Anufriev R, Hori T, Shiomi J, Volz S, Nomura M. Thermal conductivity reduction in silicon fishbone nanowires. Sci Rep 2018;8(1).
[175] Liu WL, Borca-Tasciuc T, Chen G, Liu JL, Wang KL. Anisotropic thermal conductivity of Ge quantum-dot and symmetrically strained Si/Ge superlattices. J Nanosci Nanotechnol 2001;1(1):39–42.
[176] Lee SM, Cahill DG, Venkatasubramanian R. Thermal conductivity of Si–Ge superlattices. Appl Phys Lett 1997;70(22):2957–9.
[177] Borca-Tasciuc T, Liu W, Liu J, Zeng T, Song DW, Moore CD, et al. Thermal conductivity of symmetrically strained Si/Ge superlattices. Superlattice Microst 2000;28(3):199–206.
[178] Zeng G, Shakouri A, LaBounty C, Robinson G, Croke E, Abraham P, et al. SiGe micro-cooler. Electron Lett 1999;35(24):2146.
[179] Yang B, Liu WL, Liu JL, Wang KL, Chen G. Measurements of anisotropic thermoelectric properties in superlattices. Appl Phys Lett 2002;81(19):3588–90.
[180] Li G, Yarali M, Cocemasov A, Baunack S, Nika DL, Fomin VM, et al. In-plane thermal conductivity of radial and planar Si/SiOx hybrid nanomembrane superlattices. ACS Nano 2017;11(8):8215–22.
[181] Grimm D, Wilson RB, Teshome B, Gorantla S, Rümmeli MH, Bublat T, et al. Thermal conductivity of mechanically joined semiconducting/metal nanomembrane superlattices. Nano Lett 2014;14(5):2387–93.
[182] Hachichi K, Lami A, Zemmouri H, Cuellar P, Soni R, Ait-Amar H, et al. Silicon recovery from kerf slurry waste: a review of current status and perspective. Silicon. 2017.
[183] Mehta Shyam. PV technology and cost outlook, 2013-2017. 2013. June [cited] Available from: https://www.greentechmedia.com/research/report/pv-technology-and-cost-outlook-2013-2017.
[184] Fischer M. International technology roadmap for photovoltaic (ITRPV). ninth ed. 2018. March 2018.
[185] Drouiche N, Cuellar P, Kerkar F, Medjahed S, Boutouchent-Guerfi N, Ould Hamou M. Recovery of solar grade silicon from kerf loss slurry waste. Renew Sustain Energy Rev 2014;32:936–43.
[186] Lin Y-C, Wang T-Y, Lan C-W, Tai CY. Recovery of silicon powder from kerf loss slurry by centrifugation. Powder Technol 2010;200(3):216–23.
[187] Li J, Huang K, Zhu H. Phase separation of a microsized powder mixture of Si and SiC by Cu–Si alloying. Chem Eng Sci 2015;127:25–30.
[188] Moen M, Halvorsen T, Mørk K, Velken S. Recycling of silicon metal powder from industrial powder waste streams. Met Powder Rep 2017;72(3):182–7.
[189] Akasaka M, Iida T, Mito Y, Omori T, Oguni Y, Yokoyama S, et al. Fabrication of Mg2Si from a reused-silicon source and its thermoelectric characteristics. MRS Proceedings 2011:1044.
[190] Honda Y, Iida T, Sakamoto T, Sakuragi S, Taguchi Y, Mito Y, et al. Direct thermal-to-electric energy conversion material consisting of environmentally-benign Mg2Si synthesized using waste Si sludge and recycled Mg alloy. MRS Proceedings 2011:1218.
[191] Isoda Y, Tada S, Kitagawa H, Shinohara Y. Thermoelectric properties of Sb-doped Mg2Si prepared using different silicon sources. J Electron Mater 2015;45(3):1772–8.
[192] Mesaritis G, Symeou E, Delimitis A, Oikonomidis S, Jaegle M, Tarantik K, et al. Recycling Si-kerf from photovoltaics: a very promising route to thermoelectrics. J Alloy Comp 2018;775:1036–43.
[193] Harris GL. Properties of silicon carbide. Iet; 1995.
[194] May AF, Singh DJ, Snyder GJ. Influence of band structure on the large thermoelectric performance of lanthanum telluride. Phys Rev B 2009;79(15).
[195] Kim H-S, Gibbs ZM, Tang Y, Wang H, Snyder GJ. Characterization of Lorenz number with Seebeck coefficient measurement. Apl Mater 2015;3(4), 041506.
[196] Nakamura Y, Isogawa M, Ueda T, Yamasaka S, Matsui H, Kikkawa J, et al. Anomalous reduction of thermal conductivity in coherent nanocrystal architecture for silicon thermoelectric material. Nanomater Energy 2015;12:845–51.

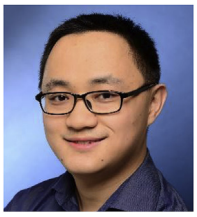

Ran He currently works as a postdoc at IFW-Dresden. He got his Bachelor degree in material physics in 2011 from Northeastern University in China. He studied physics at Boston College till the end of 2012, and then transferred to the University of Houston and obtained his Ph.D. degree in physics in 2016. His research interest mainly focuses on the transport properties of electron and phonon in mid-to-high temperature thermoelectric materials.

Wieland Heyn studied materials science at the TU Dresden from 2012 to 2018. In 2018 he finished his Diploma thesis at the IFW-Dresden. The topic was the thermoelectric characterization of n-doped industrial silicon-sawing-wastes. In April 2018 he started to work at the IKTS-Dresden as a PhD-student. His study focuses on the mechanical characterization via nanoindentation of back-end-of-line-structures in microelectronic products.

Felix Thiel works as a Ph.D. student at the IFW Dresden. He studied materials science and engineering at the Freiberg University of Mining and Technology. Between 2012 and 2013 he worked as a trainee at the Technical University of Denmark for 5 Month. He achieved his diploma degree from the TU Freiberg in 2015. His scientific activity is mainly focused on the structure-property-relationship in high-entropy alloys.

Nicolás Pérez works as a postdoc fellow at IFW Dresden since 2014. He obtained his degree in Physics (1999) at the Universidad de La Laguna, MBA (2002) at the MBA Business School, Master in Nanoscience and Nanotechnology (2007) at the Universitat de Barcelona, and PhD in Nanoscience (2012). His research interests include functional materials (magnetic, thermoelectric, magnetocaloric), and their application to energy and biomedicine.

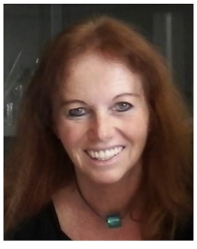

Christine Damm got her diploma in materials science in the year 1976. Since then she has been involved in the characterization of metallic materials, especially TEM investigations in the IFW Dresden.

Darius Pohl currently works as a senior scientist at the Dresden Center for Nanoanalysis, TU Dresden. He worked as a Post Doc at the IFW-Dresden from 2013 till 2018. He got his Ph.D. degree in physics in 2013 from TU Dresden, Germany. His study mainly focuses on transmission electron microscopy, nanomaterials and magnetism.

Bernd Rellinghaus has earned his PhD in physics from the University of Duisburg, Germany, in 1995. After a period as a postdoc at the IBM Almaden Research Center in San Jose, CA, USA (1995–1996), he returned to the University of Duisburg as a research assistant, before he accepted a position as Department Head at the Leibniz Institute for Solid State and Materials Research Dresden e.V. (IFW Dresden, 2004 to 2017). Since 2018 he serves as the Director of the Dresden Center for Nanoanalysis (DCN) at the TU Dresden. Bernd Rellinghaus is an expert in aberration-corrected high resolution analytical transmission electron microscopy, structure-property relations, nanoparticles, metallic materials, and (nano)magnetism.

Christian Reimann studied Mineralogy at the Johannes Gutenberg University Mayence and University Cologne. Since 2005 he has been a research scientist at Fraunhofer IISB and received his Ph.D. from Friedrich-Alexander University Erlangen-Nuremberg in 2010. In 2010 he became manager of the silicon group and in 2016 Deputy Head for the Materials Department at Fraunhofer IISB.

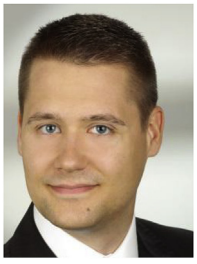

Maximilian Beier studied material science at Friedrich-Alexander University (FAU) Erlangen-Nuremberg and got his master degree in 2014. Since 2014 he has been a research scientist at Fraunhofer IISB working in the silicon group.

Jochen Friedrich studied material science at Friedrich-Alexander University (FAU) Erlangen-Nuremberg and received his Ph.D. in 1996. Since 1998 he has been a research scientist at Fraunhofer IISB working on different fields of semiconductor material development. Since 2003 he became Head of the Materials Department at Fraunhofer IISB.

Hangtian Zhu is currently a postdoc fellow in the Department of Physics and TcSUH at the University of Houston, USA. He obtained his PhD degree from University of Science and Technology Beijing, China. His current research mainly focus on novel half-Heusler thermoelectric materials.

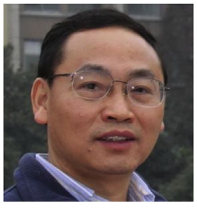

Dr. Zhifeng Ren is currently an M.D. Anderson Chair Professor in the Department of Physics and TcSUH at the University of Houston. He obtained his Ph.D. degree from the Institute of Physics Chinese Academy of Sciences, master degree from Huazhong University of Science and Technology, and bachelor degree from Sichuan Institute of Technology. He was a postdoc and research faculty at SUNY Buffalo before joining BC as an Associate Professor in 1999. He specializes in thermoelectric materials, solar thermoelectric devices, photovoltaic materials and systems, carbon nanotubes and semiconducting nanostructures, nanocomposites, bio agent delivery and biosensors, flexible transparent conductors, superconductors, etc.

Kornelius Nielsch has studied physics at the University Duisburg. For Ph.D. he joined the Max-Planck-Institute Halle. In 2002, he was a postdoctoral associate at MIT for one year. Before he was appointed as professor for experimental physics by Hamburg University in 2006, he has managed a research group in Halle. From 2009 until 2016 Nielsch has coordinated the German Priority Program on Nanostructured Thermoelectrics. In 2015, he became the director at the IFW Dresden.

Gabi Schierning received her Ph.D. degree in 2005 from the University of Erlangen-Nuremberg, Germany. After postdoc positions, she then worked at the University of Duisburg-Essen and was group leader of an independent young researcher group working on nanostructured thermoelectric mate-rials from 2009 to 2015. In 2015, she joined the Leibniz Institute for Solid State and Materials Research Dresden (IFW Dresden) as head of the department thermoelectric materials and devices.